Sahyadri International Journal of Research

VOL.2 ISSUE 2 ISSN 2456-186X DECEMBER 2016

Research Papers

Review Papers

Scientific Articles

SAHYADRI
COLLEGE OF ENGINEERING & MANAGEMENT
MANGALURU

Contents

Contents

Editorial 27

Research / Review Articles

Numerical Investigations of a Novel Sliding Support Cantilever Design for Vibration Energy Transduction 28-31

Design and implementation of high speed FIR filter using CSD multiplier algorithm on FPGA's 32-35

Plane Stress Analysis of Layered Composite Plate subjected to varying in-plane patch load 36-40

Whispering Gallery Mode Resonators at Optical and Terahertz Frequencies: A Brief Review 41-50

Effects of Corrugation Profile on the Heat Transfer Rate of Fins 51-56

Study of Effect of Heat Treatment Processes On Material Properties of Manganese Steels 57-61

Scientific Articles

Search for the value of π - A brief history 62-63

General Guidelines 64

SAHYADRI
International Journal of Research
Vol. 2, Issue 2
ISSN 2456-186X (Online)
ISSN Pending (Print)

Mailing Address:
Editor
Sahyadri International Journal of Research
Sahyadri campus, Adyar,
Mangalore - 575 007, India
E-mail: editor@sijr.in
Website: www.sijr.in

Editorial

Sahyadri International Journal of Research (ISSN: 2456-186X) is a journal covering wide disciplines of science, engineering and technology. SIJR is published biannually and is an open access journal available online.

It gives us immense pleasure to bring out Volume 2, Issue 2 of SIJR. However, there are lots of challenges in bringing out a high quality research journal. Our focus is multidisciplinary; the most important disciplines in which we would focus are Physics, Chemistry, Applied mathematics, Electronics and Communication, Mechanical Engineering, Civil Engineering and Computer Science and Engineering. Apart from research papers, the journal also would publish articles on important scientific discoveries. The current issue has research articles, review papers and a scientific article.

Editorial team would like to thank the contributors and reviewers of Volume 2, Issue 2.

- Editorial Board

Research Paper

Numerical Investigations of a Novel Sliding Support Cantilever Design for Vibration Energy Transduction

R. Rathishchandra Gatti
Mechanical Engineering Dept., Sahyadri College of Engineering & Management, Adyar, Mangalore-575007
Email: rathishchandra.mech@sahyadri.edu.in

Abstract

Cantilever topologies are very commonly used in energy transduction mechanisms which involved cyclic dynamic loads such as frequency tachometers for detecting the vibration frequency or energy harvesters for generating energy from wasted vibrations. Another advantage of the cantilever topology is its scalability to MEMS level compared to other spring structures such as helical and leaf springs etc. The natural frequency of the cantilever depends on its length and this factor is utilized here to envisage a novel topology for construction of energy transducers. A numerical investigation using finite element analysis is initially done to understand the variation of the natural frequency with respect to the changing length for a single cantilever beam. This is cross validated using analytical results.

Keywords: Cantilever, broadband, energy transduction, varying length, electromagnetic, piezoelectric, power harvesting, energy harvester, micro-electromechanical systems, biosensors, sensors.

1 Introduction

Recent advances in energy harvesting transducers and vibration sensors have necessitated the scientists to try for different topological approaches to transduce vibration energy into electrical energy [1]. Cantilever beam structures are commonly used in converting vibration energy to usable electrical energy such as those found in piezoelectric vibration energy harvesters [2] and sensors such as Micro-electromechanical systems (MEMS)biosensors [3]. One of the key interests of the vibration energy harvesting research is the ability of the energy harvesters to generate power for a range of frequencies for which several topologies have been investigated and reported. A few techniques include frequency up-conversion [4], spatially varying the magnetic field [5], using non-linear oscillators [6] to name a few. This key design requirement of broadband energy harvesting is addressed in the proposed design.

In the proposed design, a lumped mass single degree of freedom spring mass damper system is proposed where the spring is a cantilever fixed at one end and the lumped mass suspended on the free end. The novelty in the proposed design is a sliding support or base that varies the overhanging length of the cantilever thus leading to the desired natural frequency. The inspiration for the proposed design is the design of Fullerton tachometer wherein the length of the suspended cantilever is adjusted by a screw in between the fixed structure and the free end with lumped mass. Another inspiration for the proposed design are the promising results of the feasibility of creating sliding contacts in MEMS as discussed by Ingrid Ku [7]. One important tribological design constraint is to minimize the frictional wear while designing sliding MEMS contacts since the surface friction coefficient is high due to high surface to volume ratio in MEMS structures. This can be minimised to acceptable levels of $\mu = 0.05$ to 0.1 for less than 100rpm by using low viscosity lubricants such as Octadecylamine 0.1% in Silicon oil [7].

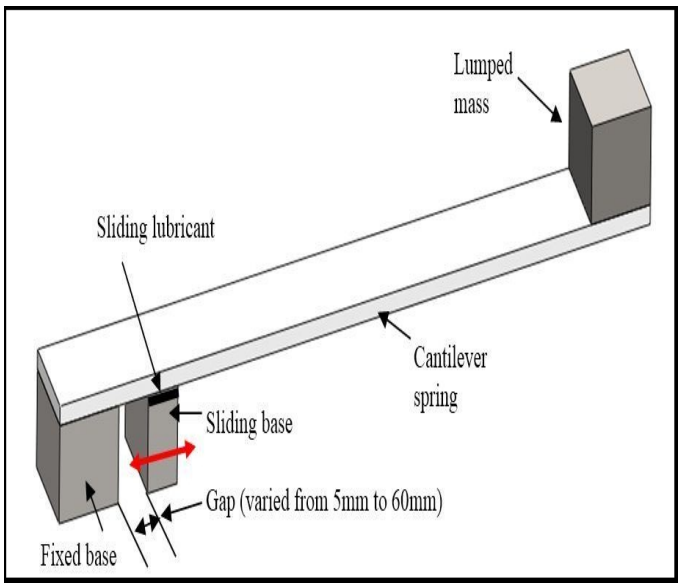

Figure 1: Sliding support cantilever design.

Since the sliding speed does not exceed as high as linear equivalent of 1000 rpm where $\mu > 0.2$, it is assumed that sliding MEMS contacts are feasible to go ahead with the proposed design.

2 Design

The sliding support cantilever design is as shown in the Figure 1. It consists of a cantilever spring made of a flexible material. The spring is supported on two supports - a fixed base and a sliding base. A lumped mass is

suspended on the free end of the cantilever spring.

The natural frequency of the cantilever with free ends is given by,

$$f_n = \frac{1}{2\pi}\sqrt{\frac{3EI}{ml^3}} \quad (1)$$

where E = modulus of elasticity of the cantilever beam, I = mass moment of inertia, m = mass of the lumped mass suspended, l = overhanging length of the cantilever beam. In the proposed design, the length l can be varied by increasing the gap between the fixed base and the sliding base.
Commonly available materials such as PET for cantilever spring, plain carbon steel for fixed and moving support were considered for the proposed mesoscopic design (at mm scale). At MEMS scale the choice of materials will definitely shift towards thin film polyamides and other flexible substrates for cantilevers and Silicon for lumped mass, fixed support and moving supports for the ease of fabrication. However, the scope of this study is limited to understand the dynamic behaviour and modal frequency response of this unique design rather than identification of the material selections for the MEMS fabrication which can be considered in the future work and therefore not in scope of this study. The main interest of designing any vibration energy harvester design is its ability to harvest energy over the range of frequencies from random vibrations. Hence, linear dynamic FEA analysis with random base excitation load was performed to understand and know the modal frequencies of the cantilever at different varying lengths. In the FEA simulation, the gap between the fixed support and the moving support was varied from 5mm to 60 mm in steps of 5mm.

3 Simulation

3.1 Simulation Setup

Linear dynamic FEA analysis using random vibration was performed to understand and know the modal frequencies of the cantilever at different varying lengths. In the FEA simulation, the gap between the fixed support and the moving support was varied from 5mm to 60 mm in steps of 5mm at lab temperature of 25°C.

3.2 Linear dynamic analysis simulation conditions

The entire assembly was meshed using a solid mesh using 8550 tetrahedral elements with element size of 1.652 mm and 14169 nodes as shown in Figure 2. The fixed base and the sliding base was fixed using the fixed geometry conditions. A practical average value of 2mm amplitude was considered for the base excitation load condition that was applied on the bottom surfaces of the fixed base and the sliding base. The iterative solver namely the FFEPlus solver in Solid works was used rather than the accurate direct sparse solver due to insufficient memory space and longer time required by direct sparse solver.

4 Results and Discussion

The energy transduction of the energy transducer depends on its amplitude of vibration. Also, the energy conversion is maximum when the prominent frequencies of the source of vibration are in resonance with the natural frequency of the energy transducer. The proposed design considers varying cantilever length and hence the modal frequencies of the energy transducer will also need to be observed. Hence, the post processing of the simulation results was done to obtain the stress, displacement and the modal frequencies from the linear dynamic FEA simulation.

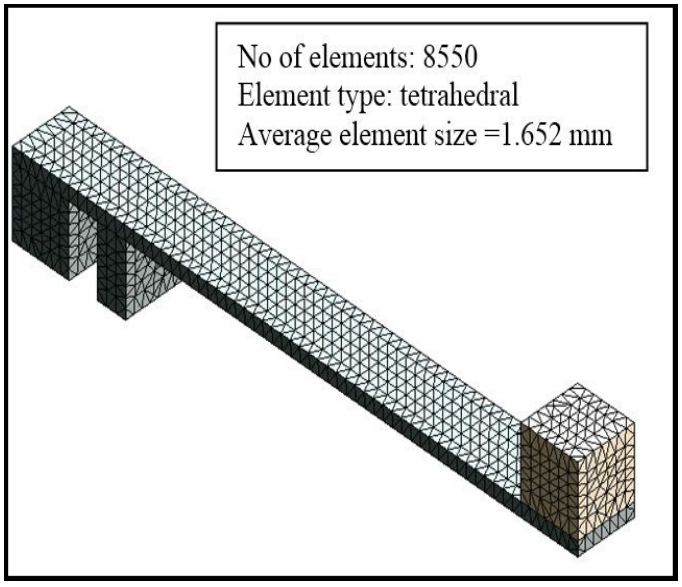

Figure 2: Finite element Mesh using Solid mesh.

4.1 Stress and Displacement results

For the design to be safe, the distortion energy theory and hence, the Von-Mises stress analysis was considered. As seen in Figure 3, the Von-Mises stress was found to be maximum at 0.0377N/m^2 and was within the limits of yield point of the cantilever spring. This was because the base displacement of 2mm was too low for inducing any high stresses at the stress zones. It was also because of the high yield strength of Plain carbon steel that was chosen for the cantilever spring.

As evident in Figure 4, the displacement of the tip of the mass was maximum. The maximum displacement of the cantilever beam is found to vary from 1.23 mm for 60mm gap to 5.76 mm for 5mm gap. The mass tip excitation to the base excitation magnification ratio was thus 1.23/2 = 0.615 for 60mm gap and 5.76/2 = 2.88 for 5 mm gap. This is true since the length of the overhang of the cantilever decreases with the increase of gap. The top down approach of the energy harvester design would be to estimate the amplitude of vibration required and then design the sliding base energy harvester to appropriate range of length variations.

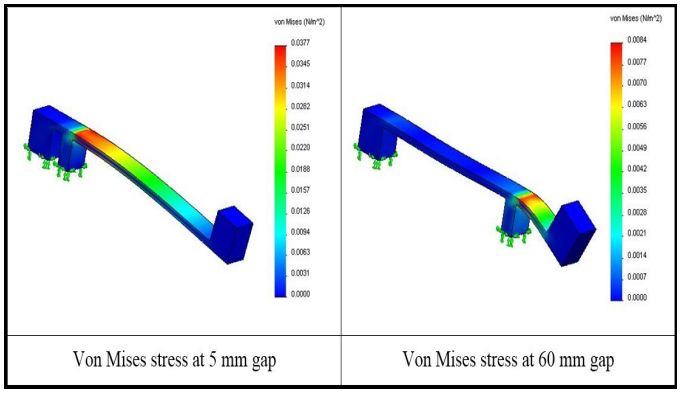

Figure 3: Von-Mises stresses shown for 2 extreme positions of sliding base.

4.2 Random vibrations modal analysis

Most of the energy harvesters based on seismic masses are designed to operate at their fundamental modes but the knowledge of higher modes is beneficial to understand the structural failure modes. The natural frequencies at the fundamental modes (fundamental natural frequencies) and the second modes is shown in the Figure 5. It can be seen that as the gap between the supports increases, the overhanging length decreases thus increasing the natural frequency which inversely depends on the overhang length. It can also be deduced from Figure 5 that one can design an energy harvester for a particular frequency range and then set the minimum and maximum limits of the gap variation between the supports in this harvester design.

As observed in Figure 6, the higher mode natural frequencies tend to vary non-linearly with the increase in gap between the supports. At mode 5, the modal natural frequencies increase up to 35 mm and then decreases which is due to buckling and the mode shapes of vibration. However, most of the practically available industrial vibrations with higher amplitudes fall within 1000 Hz and thus this will not seriously affect the energy harvester design.

4.3 Application of the proposed design

The proposed design can be used for designing piezoelectric, electrostatic, and electromagnetic or a combination of two or more of these transduction technologies. It can readily be applied to piezoelectric based energy harvesters. One concept design of a MEMS piezoelectric energy harvester is as shown in the Figure 7 below. This concept consists of a fixed base and a sliding base with low viscosity lubricants such as Octadecylamine 0.1% in Silicon oil [7] being provided between the sliding contact surfaces. The cantilever can be made of a polyamide with piezoelectric ally active properties such as PVDF-TrFE [8]. The lumped mass can be made of a high density material or the same material as that of cantilever depending on the ease of fabrication.

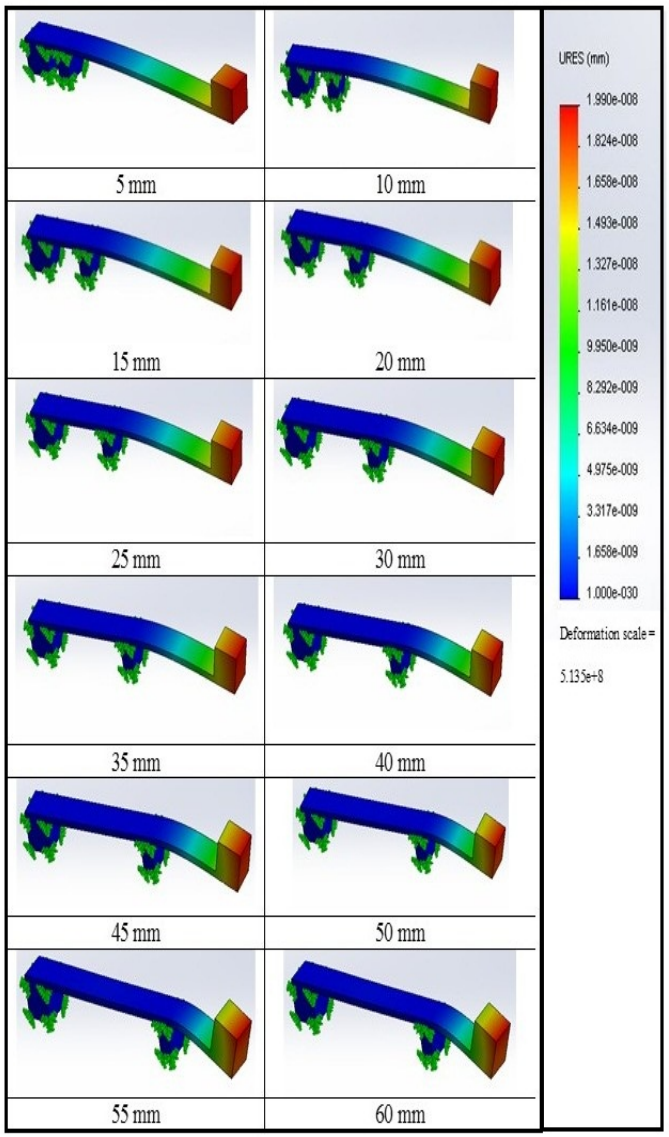

Figure 4: Displacements shown for 2 extreme positions of sliding base.

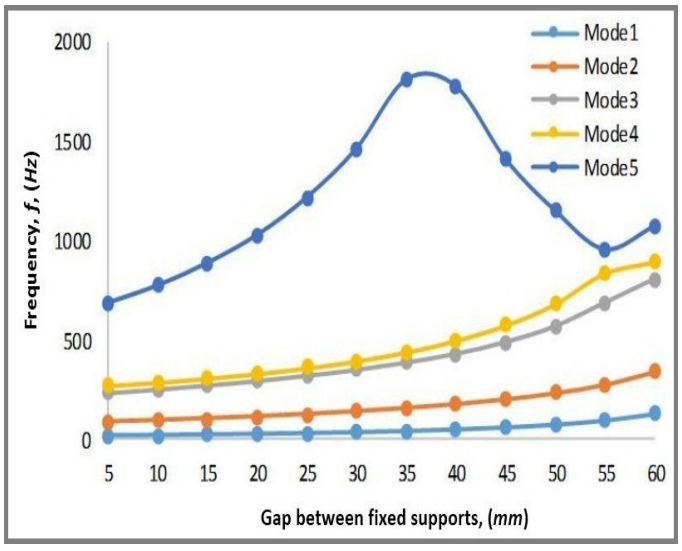

Figure 5: Modal frequencies of the sliding base cantilever at fundamental mode and higher modes.

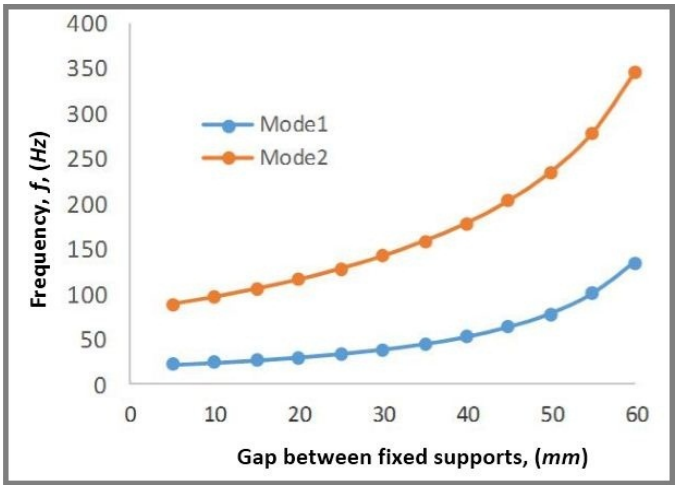

Figure 6: Modal frequencies of the sliding base cantilever at fundamental mode and secondary modes.

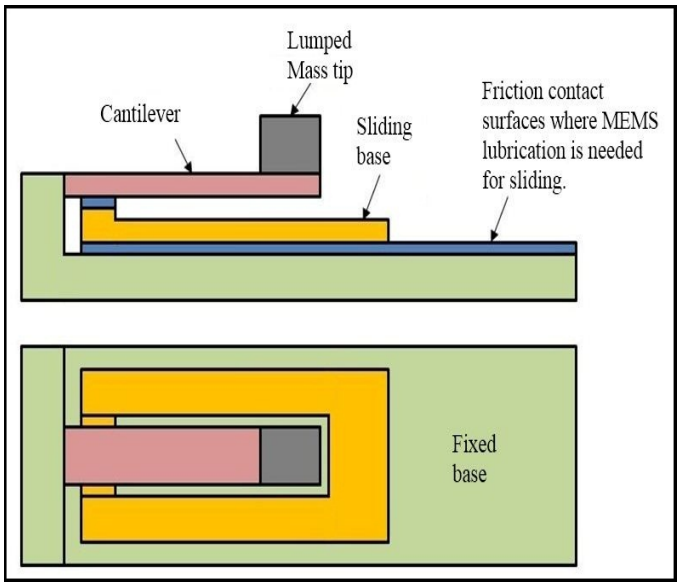

Figure 7: Concept design of a MEMS piezoelectric energy harvester.

5 Conclusion

A novel cantilever energy harvester design is proposed that consists of a fixed base and a sliding base to vary the length of the cantilever. A linear dynamic FEA analysis for random vibrations is simulated with a base excitation of 2 mm. The length of the gap is varied from 5mm to 60 mm to observe the change in natural frequency, maximum Von-Mises stress levels and maximum displacements. It was observed that an energy harvester can adopt this design to harness a range of frequencies by changing its length using the sliding contact. The future challenge is MEMS fabrication and study of tribological design considerations to reduce friction.

Acknowledgement

The author would like to thank Professor Ian M. Howard, Department of Mechanical Engineering, Curtin University, Australia for providing his in-depth knowledge and guidance in vibration energy harvesting research during the author's PhD work, which has fuelled the author's work even today.

References

[1] S. Priya and D.J. Inman, eds. "Energy harvesting technologies", New York-Springer, pp. 2-4, 2009.

[2] M. Lumentut and I. M. Howard, "Electromechanical finite element modelling for dynamic analysis of a cantilevered piezoelectric energy harvester with tip mass offset under base excitations", Smart Materials and Structures, vol. 23, pp. 095037-095061, 2014.

[3] A. Porwal, et al., "Microcantilever based biosensors", IETE Technical Review, vol. 19, pp. 257-267, 2002.

[4] M. A. Halim, H.O. Cho and J.Y. Park, "A handy motion driven, frequency up-converting piezoelectric energy harvester using exible base for wearable sensors applications", IEEE SENSORS, pp. 1-4, 2015.

[5] R. R. Gatti, "Spatially varying multi degree of freedom electromagnetic energy harvesting", PhD Thesis, Curtin University, Australia, 2013.

[6] D. A. Barton, S.G. Burrow and L.R. Clare, "Energy harvesting from vibrations with a nonlinear oscillator", J. Vibration and Acoustics, vol. 132, pp. 021009- 021016, 2010.

[7] I. Ku, "Lubrication of High sliding machines", PhD Thesis, Imperial College, London, 2010.

[8] K. R. Rashmi, S. Rai, R. R. Gatti, A. Jayarama, N. Bappalige, N. Joshi, R. Pinto and S. P. Duttagupta, "Simulation and fabrication considerations of P(VDF-TrFE) cantilevers", Sahyadri International Journal of Research, vol. 1, pp. 8-10, 2015.

Research Paper

Design and implementation of high speed FIR filter using CSD multiplier algorithm on FPGA's

G. K. Dayanand[1*], A. Jayarama[2] and C. Shantharama Rai[3]

[1]E & C Dept., Canara Engineering College, Mangalore, 574219 India

[2]Physics Dept., Sahyadri College of Engineering and Management, Adyar, Mangalore, 575007 India.

[3]E&C Dept., AJIET, Mangalore, 570006 India.

*Email: dayanand.gk@gmail.com

Abstract

A Canonic Signed Digit(CSD) algorithm for Finite Impulse Response (FIR) filters is designed and simulated in Very High Speed Integrated Circuit Hardware Description Language (VHSIC-HDL) and implemented on Spartan 2E Field-Programmable Gate Array (FPGA). The customized Integrated Circuit (IC) can be used as a potential high speed FIR filter for various applications in the field of satellite, mobile communication etc. The designed FIR filter consumes total memory of 75320 Kilobytes with frequency of 146.370MHz in Xilinx Sparten 2E kit

Keywords: FPGA, CSD , FIR Filter, VHDL.

1 Introduction

The modern technology is moving towards high speed speech processing, image compressing, digital modulation techniques which involve processing of digital signals and applications like optical fiber or wireless communication. The processing, compression and modulation of digital signal should be very fast, so that higher speed transmission can be possible [1, 2].

Digital signals can be stored and removed, transmitted and received, processed and manipulated, all virtually without error. Two major advantages that distinguish DSP from other application oriented general purpose computation processing are the real-time throughput, speed and data driven property. DSP filters are signal conditioners. Finite Impulse Response (FIR) digital filters, widely used in signal processing , are one of two primary types of digital filters used in digital signal applications; the other type is feedback oriented Infinite Impulse Response filter (IIR).

Digital filters can be implemented with less hardware using a CSD representation. For multipliers computation is commonly done by addition and shift methods. In CSD method, number of additions and shifts operations implemented for a multiplier depends on the number of non-zero binary bits in the binary digits representation. Extracting common sub-computations between the filter coefficients can minimize the number of additions and shift operations [3, 4]. This realizes an area-efficient implementation of the filter. Coefficient transform are very important in realizing area-efficient multiplier. By applying coefficient transform in combination with subexpression and pre-computation technique, we can save many additions and subtractions. Strength reduction at the algorithm level can be used to reduce the number of additions. An efficient algorithm is represented by the reduced finite digital filter coefficients, which are represented by a Canonical Signed Digits numbers representation, i.e., numbers represented as sums or subtraction of power-of-two [5].

Recent interest is in using minimum adder/subtracter units for multiplier. The design and implementation of digital filters has extensively contributed to future development using CSD number system [6,7]. The integer coding schemes considered here belong to a class of numbers called fixed point. Fixed point refers to the fact that the binary point is found in fixed location. There exist a few other fixed point systems, which hold some interest to the digital signal processing scientists. One of such system is called the canonical signed digit code. In the early 1950's, this code enjoyed a high degree of popularity.

A common method of carrying out multiplication is by addition and shifting operations of constant numbers. By optimized hardware utilization, it is possible to alter this method by addition or subtractions. The CSD method has the benefits of reducing the number of additions/subtractions, in addition to effortlessly handling negative multipliers; results are obtained by representing the multiplier in CSD form. In this paper we report, design of high-speed computation FIR filters using CSD based multiplier implemented on FPGA's for DSP applications. DSP systems can be realized using programmable processors or custom designed hardware circuits fabricated using very large scale integration (VLSI) circuit technology.

1.1 CSD algorithm

An algorithm for computing the CSD format of a W-bit number is presented below. Denoted below is the two's compliment representation of the number A as A=$\hat{a}_{w-1}$. $\hat{a}_{w-2}$, ...$\hat{a}_1$,$\hat{a}_0$ and its CSD representation of the number A=a_{w-1}. a_{w-2}, ...a_1,a_0, the conversion is illustrated using the following iterative algorithm: $\hat{a}_{-1}$=0
γ_{i-1}=0
$\hat{a}_w$= $\hat{a}_{w-1}$
for(i= 0 to W-1)
{ θ_i = $\hat{a}_i$ xor $\hat{a}_{w-1}$
γ_i = not(γ_i) θ_i
$\hat{a}_i$ = (1-2 $\hat{a}_{i+1}$) γ_i }

An example for CSD algorithm is given in table 1; the input number is 1.01110011 and its CSD representation is given by a_i.

Table 1: CSD representation a_i

i	W	W-1	...							0	-1
$\hat{a}_i$	1	1	0	1	1	1	0	0	1	1	0
θ_i		1	1	0	0	1	0	1	0	1	
γ_i		0	1	0	0	1	0	1	0	1	0
(1-2$\hat{a}_{i-1}$)		-1	-1	-1	-1	-1	-1	1	1	-1	
$\hat{a}_i$		0	1	0	0	-1	0	1	0	-1	

2 Design and Implementation

The applications of high speed digital filtering (> 10MHz) normally necessitate the use of defined application specific integrated circuits (ASIC's). User programmable signal processor cannot handle such huge computation of sample rates devoid of an extreme amount of parallel or hybrid processing which is expensive. For user defined applications flexibility of a multiplier is unnecessary. Hence , more optimized filter modules can be obtained by implementing each filter coefficient with selected arithmetic elements which recognize a particular filter coefficient. Multiplication process by power-of-two is obtained in user defined hardware structure by left-shifting or right-shifting of the data bus to a proper number of adders/substractors in each filter taps for digital filters along with suitable shifting operation. The ensuing hardware complication is a minimal fraction of the intricacy of a general-purpose multiplier and thus a more numbered complex of filter taps can be designed and implemented onto a single IC.

The numbers representing sum/subtractor of power-of-two is properly known as radix-2 signed binary digit code. The radix-2 representing signed-digit in fractional number x has following general form as shown in equation 1.

$$x = \sum_{k=0}^{L} a_i 2^{-pi} \tag{1}$$

Where $a_i \in$ {0,1,-1} and pi $\in$ {0,1,. . . .,N}. The representation has N+1 total number digits and l nonzero digit. In general there are many signed digits symbols for a given number.

3 Results and Synthesis Report

CSD algorithm was successfully continued for filter containing 30 coefficients of 16 bits binary chosen at random. The results are shown in table-2 and the coefficients are represented by 2's power format as shown in table 3.

The entity of design is shown in figure 1 with input output ports ; master_clk is clock signal for entire design; cl_en is clock enable and rst is reset pin. The fir_in is n-bit input samples and fir_out is n-bit samples convoluted with coefficients. VHDL code for FIR filter using CSD algorithm has been successfully implemented on FPGA (Xilinx Spartan 2E); the place and mapping is as shown in figure 2. The output waveforms of 30-tap low pass filter is shown in figure 3. Synthesis and timing summary reports are shown in in table 4 , the circuit will work at maximum frequency of 146.370MHz; Total memory usage is 75320 kilobytes.

Table 2: Original FIR filter coefficients.

h[0]	0.008021
h[1]	0.009826
h[2]	0.011483
h[3]	0.008938
h[4]	0.000996
h[5]	-0.011612
h[6]	-0.025746001
h[7]	-0.036224999
h[8]	-0.037126999
h[9]	-0.023705
h[10]	0.005686
h[11]	0.048388001
h[12]	0.097474001
h[13]	0.143259004
h[14]	0.175752997
h[15]	0.187501997
h[16]	0.175752997
h[17]	0.143259004
h[18]	0.097474001
h[19]	0.048388001
h[20]	0.005686
h[21]	-0.023705
h[22]	-0.037126999
h[23]	-0.036224999
h[24]	-0.025746001
h[25]	-0.011612
h[26]	0.000996
h[27]	0.008938
h[28]	0.011483
h[29]	0.009826

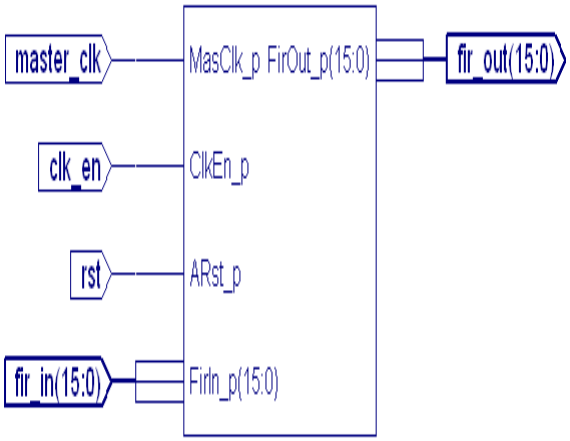

Figure 1: Entity of FIR filter

Table 3: CSD Filter Coeffecients

h[0]	2^-5	0.00390625	-0.001953125	2^-15	0^0	0^0	0^0	0^0	0^0	
h[1]	2^-5	-0.00012207	0^0	0^0	0^0	0^0	0^0	0^0	0^0	
h[2]	2^-5	2^-8	2^-10	2^-12	0^0	0^0	0^0	0^0	0^0	
h[3]	2^-5	0.00390625	2^-10	0^0	0^0	0^0	0^0	0^0	0^0	
h[4]	2^-8	0.000976563	2^-12	-3.05176E-05	0^0	0^0	0^0	0^0	0^0	
h[5]	-2^-5	0.00390625	-0.001953125	2^-12	2^-14	2^-15	0^0	0^0	0^0	
h[6]	-2^-4	0.015625	0.00390625	2^-11	-3.05176E-05	0^0	0^0	0^0	0^0	
h[7]	-2^-3	2^-7	2^-9	2^-11	0^0	0^0	0^0	0^0	0^0	
h[8]	-2^-3	2^-7	-0.000488281	2^-14	0^0	0^0	0^0	0^0	0^0	
h[9]	-2^-4	0.015625	2^-8	0.000976563	2^-13	-3.05176E-05	0^0	0^0	0^0	
h[10]	2^-6	2^-9	2^-11	6.10352E-05	0^0	0^0	0^0	0^0	0^0	
h[11]	2^-3	2^-5	0.00390625	2^-10	-3.05176E-05	0^0	0^0	0^0	0^0	
h[12]	2^-2	2^-4	0.00390625	2^-12	-3.05176E-05	0^0	0^0	0^0	0^0	0^0
h[13]	2^-1	-0.03125	0.015625	2^-11	2^-12	-3.05176E-05	0^0	0^0	0^0	0^0
h[14]	2^-1	2^-4	0.00390625	-0.001953125	2^-13	2^-15	0^0	0^0	0^0	0^0
h[15]	2^-1	2^-3	-0.03125	2^-12	0^0	0^0	0^0	0^0	0^0	0^0
h[16]	2^-1	2^-4	0.00390625	-0.001953125	2^-13	2^-15	0^0	0^0	0^0	0^0
h[17]	2^-1	-0.03125	0.015625	2^-11	2^-12	-3.05176E-05	0^0	0^0	0^0	0^0
h[18]	2^-2	2^-4	0.00390625	2^-12	-3.05176E-05	0^0	0^0	0^0	0^0	0^0
h[19]	2^-3	2^-5	0.00390625	2^-10	-3.05176E-05	0^0	0^0	0^0	0^0	
h[20]	2^-6	2^-9	2^-11	6.10352E-05	0^0	0^0	0^0	0^0	0^0	
h[21]	-2^-4	0.015625	2^-8	0.000976563	2^-13	-3.05176E-05	0^0	0^0	0^0	
h[22]	-2^-3	2^-7	-0.000488281	2^-14	0^0	0^0	0^0	0^0	0^0	
h[23]	-0.125	2^-7	2^-9	2^-11	0^0	0^0	0^0	0^0	0^0	
h[24]	-2^-4	0.015625	0.00390625	2^-11	-3.05176E-05	0^0	0^0	0^0	0^0	
h[25]	-0.03125	0.00390625	-0.001953125	2^-12	2^-14	2^-15	0^0	0^0	0^0	
h[26]	2^-8	0.000976563	2^-12	-3.05176E-05	0^0	0^0	0^0	0^0	0^0	
h[27]	0.008938									
h[28]	0.011483									
h[29]	0.009826									

4 Conclusion

The CSD algorithm is successfully implemented on Spartan 2E FPGA . The major factors that influence our choice of a specific realization are Computational complexity, Memory requirements and finite-word-length effects. From above method there is significant reduction in the filter complexity, minimal hardware and high speed of computation. Complexity of filter increases, with minimal changes in CSD representation which reduces the number of steps involved. There is significant frequency response also obtained from this algorithm. This method may be used in concurrence with other algorithm techniques for optimized digital FIR filter complexity like pre-filter module or the interpolated digital FIR filters. Further, same algorithm can be implemented for infinite response digital filters. Clock frequency (masclk_p) =146 MHz; Enable (cken_p) =1; Reset (arst_p)=0; Filter input(firin_p)= Sample in; Filter output (firout_p)

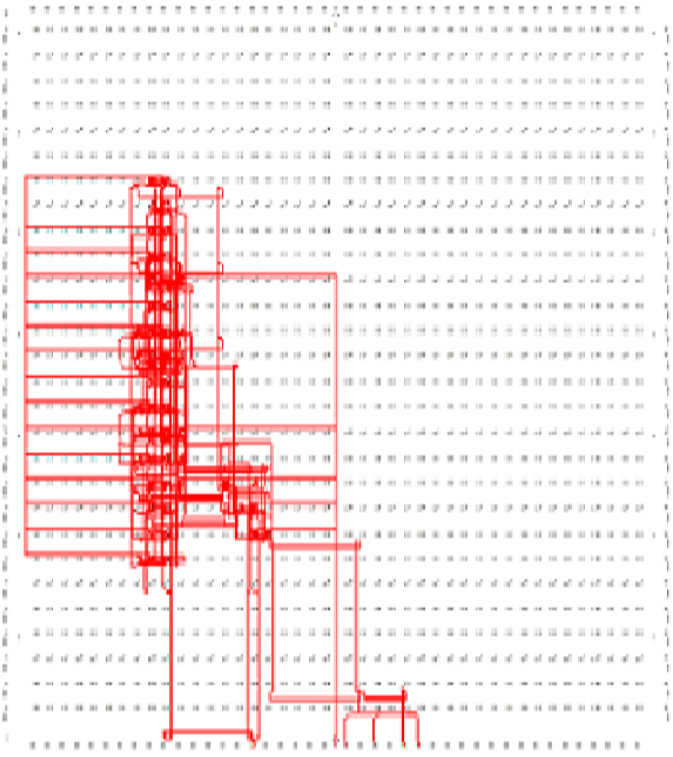

Figure 2: Placement & routing on Spartan 2E FPGA

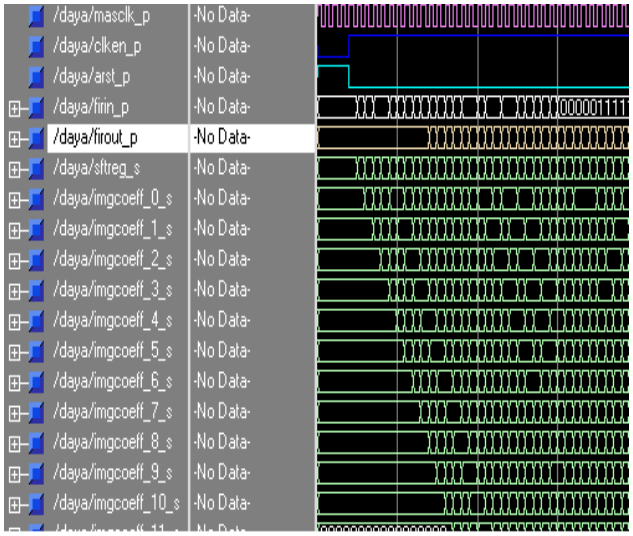

Figure 3: Output waveform of FIR pass filter

Table 4: Synthesis report and Device utilization summary

Selected Device : 2s100pq208-5 Speed Grade: -5	
Number of Slices	821 out of 1200 (68%)
Number of Slice Flip Flops	1436 out of 2400(59%)
Number of 4 input LUTs	947 out of 2400(39%)
Number of bonded IOBs	34 out of 144(23%)
Number of GCLKs	1 out of 4(25%)
Timing Summary	
Minimum period	6.832ns
Max Frequency	146.370MHz
Minimum input arrival time before clock	16.513ns
Maximum output required time after clock	7.999ns
Total memory usage	75320 Kilobytes

References

[1] F. J. Taylor, "Digital Filter Design Hand book", Marcel inc., NYC,1984.

[2] K. Keshab Pahri, “VLSI Digital Signal Processor Design and Implementation", WSE Wiley 2004 Edition.

[3] G. K. Ma and F. J. Taylor, “Multiplier policies for digital Signal processing”, IEEE ASSP Mag.vol 21, pp. 6-20, 1990.

[4] W. J. Oh and Y. H. Lee, “Implementation of programmable multiplier less FIR filters with powers-of-two coefficients,” IEEE Trans. On CAS II, vol.42, pp.553-555, 1995.

[5] R. Hartley, “Optimization of canonic signed digit multipliers for filter design”, Int. symp. circuits syst., Singapore, pp. 1992-1995, 1991.

[6] M. Reid Hewlitt, “Canonical signed digit representation for Fir digital Filters”, IEEE Workshop on Signal Processing Systems, pp. 416-426, 2000.

[7] Murko Kosunen and Kuri Halonen, ”Multiplier and shift using signed digit representations”, Patent No. US 7,257,609 B1, Date of Patent: Aug 14, 2007.

Research Paper

Plane Stress Analysis of Layered Composite Plate subjected to varying in-plane patch load

P. Sasha Rai, K. Sunil Kumar* and D. L. Prabhakara
Civil Engineering Dept., Sahyadri College of Engineering & Management, Adyar, Mangalore-575007
*Email: sunil.civil@sahyadri.edu.in

Abstract

Composites are very successful in resisting the depletion brought about by excessive dynamic conditions. Despite the fact that the segments made out of composites are lean, in view of its stiffness and high strength properties they are widely utilized. This paper aims at the comparison of each in-plane stress against corresponding allowable stresses within a lamina which makes use of maximum stress criterion method. In a lamina, when the stress value at a material point exceeds fiber strength the failure along the fiber direction is declared. Similarly, when the corresponding stress value exceeds matrix normal strength the failure in transverse direction to fiber within a lamina is confirmed. Applying the finite element analysis the first ply failure in multi-layered composites is determined. As a part of this work an in-house code was developed using Mat Lab script. An adaptive mesh was considered to account for in-plane stress concentrations in the laminate. A mesh sensitivity study was also conducted to ensure convergence of solution for the problem domain. Validation of the formulation and implementation was conducted by utilizing different loading conditions. In particular, a transverse load was applied and the deflection was compared against closed form solution to ensure correctness.

Keywords: finite element, plane stress, deflection, isotropic, along fiber direction, across fiber direction.

1 Introduction

In the last few decades composite materials have become a paramount engineering material in various fields. Composite materials have a lower shear modulus in comparison with the extensional rigidity which makes the material weak in shear. Hence, the role of transverse shear is a requisite in composites. Therefore, precise perception of structural behaviour of composites such as displacements and stresses is required. In the present work, the aim of study is to inspect maximum stress in the composite plates under varying loading. To calculate the laminate-stresses in a laminated composite plate a model in finite element with five degrees of freedom is developed and studied.

The present study aims at understanding about the failure mechanisms and to draw an algorithm for the process of analysis and also to write the required code in MATLAB.

The main objectives of this study are the following:
a) To perform plane stress analysis of composite laminate subjected to a wide variety of loads;
b) To identify the first failure location of position and the layer number;
c) To perform a parametric study of width of edge load on stress distribution and to present graphically in the form of contours.

2 Methodology

Initially the stiffness matrix in principal material direction for each lamina is worked out which has been transformed to the global direction. Stiffness matrix is initiated for the whole laminate by using Mindlin theory. By selecting the proper shape functions eight nodded isoparametric element is applied to develop strain displacement matrix for an element. Element stiffness matrix is generated by making use of displacement [B] and strain displacement matrix [C],

$$[k_p]_e = [B]_j^T [C]_j [B]_j \, dA \tag{1}$$

where k_p is stiffness matrix and dA is area of the element. Strain energy U_lp due to linear strain is given by

$$U_lp = \frac{1}{2} \sum_{j-1}^{m} \{ \bar{d} \}_j^T [k_p]_e \{ \bar{d} \}_j \tag{2}$$

in which $\bar{d}\}_j$ is displacement vector for j^{th} element.

The above summations are made in the sense of finite element assemblage, taking the global displacement vector to be d, which results in the following relation.

$$U_lp = \frac{1}{2} \{ d \}^T [k_p]_e \{ d \} \tag{3}$$

in which $[k_p]_e$ is the structure or global elastic stiffness matrix for the plate. If Π is potential energy then using the principle of minimum potential energy, variation of Π should be minimum.

or

$\delta\Pi = 0;$

or

$$\delta\Pi = \{\delta d\}^T [k_p] \{d\} - \{\delta d\}^T \{F\} = 0 \tag{4}$$

or

$$\delta\Pi = \{\delta d\}^T \left[[k_p] \{d\} - \{F\} \right] = 0 \tag{5}$$

since δd is arbitrary, it cannot be zero.

Hence,

$$[k_p]\{d\} - \{F\} = 0 \quad (6)$$

or

$$[k_p]\{d\} = \{F\} \quad (7)$$

where F is the lateral load vector, and d is the displacement vector. This is the governing equation for the plane stress analysis.

Strain at every Jacobian point is generated by using displacement vector. Extrapolation is done for mid-plane strains at jacobian points to the four corner nodes of corresponding element. Generation of stresses at all the nodes by using strain at each layer and corresponding modified reduced stiffness matrix, $\sigma = Q\epsilon$ [1, 2].
The average stresses at every node in each layer are found by making use of top and bottom stresses of four corners. Stresses are transformed from global directions to stresses along and across the fiber direction. Stress distribution is studied by plotting the stress contours.

3 Results and Discussion

The 8-nodded isoparametric element with each node of five degrees of freedom is considered. The plate is divided into 10x10 elements and each element has 8 nodes as in figure 1, which shows node numbering in mesh of 10x10 for a composite plate of size 100x100.
The discussion on classical and numerical formulation of the problem pertaining to the present study has been done. After ensuring the validation of coding and formulation, detailed studies have been carried out for lamina failure and stress contours are developed for a plate with 10 x 10 elements.

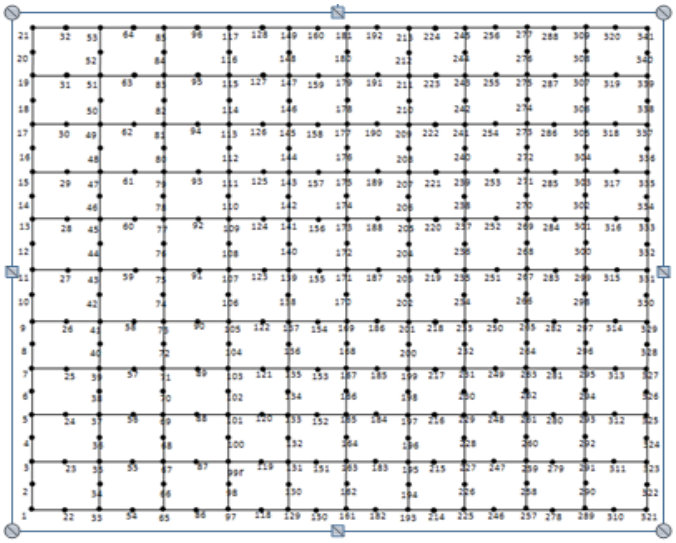

Figure 1: Node numbering in mesh of 10x10 for a composite plate of size 100x100.

Figure 2 shows geometrical configuration of laminated plate.
alx - Dimension of plate along x direction
bly - Dimension of plate along y direction
atz - Thickness of Plate
D - Flexural rigidity, $D = \frac{E(atz)^3}{12(1-\vartheta^2)}$ for isotropic plate [3] and $D = \frac{E_{22}(atz)^3}{12(1-\vartheta_{12}^2)}$ for composite plate.
nx - number of divisions in x-direction
my - number of divisions in y-direction
E_{11} - Young′s modulus in the fiber direction
E_{22} - Young′s modulus in the lateral direction of the fiber
G_{12} - in-plane shear modulus
ν_{12} - major Poisson′s ratio
θ - orientation of fiber in a layer
α - plate aspect ratio, (alx)/(bly)
β - plate width to thickness ratio, bly/atz

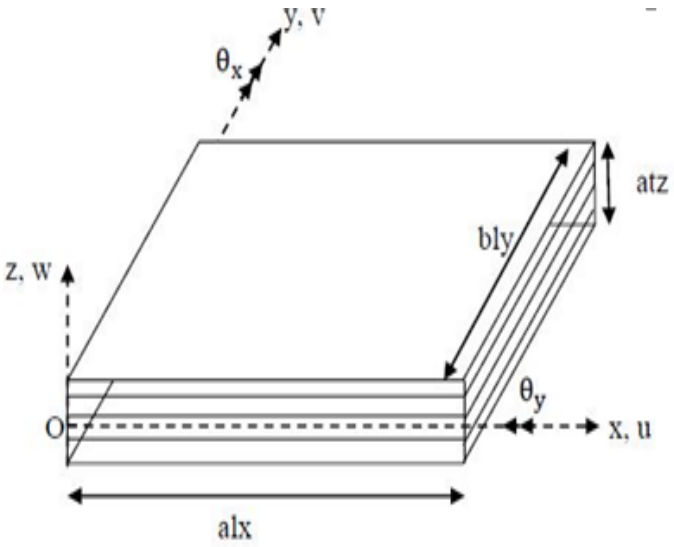

Figure 2: Geometrical configuration of laminated plate.

Table 1: Material properties.

2*Material	Material Constants		
	υ_{12}	G_{23}	G_{13}
Composite (M-1)	0.25	$0.5E_2$	$0.6E_2$
Isotropic (M-2)	0.30	0.3846	0.3846
2*	Material Constants		
	G_{12}	E_2	E_1
Compositer (M-1)	$0.6E_2$	1.0	40.0
Isotropic (M-2)	0.3846	1.0	1.0

The load application on a cantilever plate of size 100x100 is shown in figure 3. Table 1 gives the material properties of isotropic as well as composite plates.

3.1 Validation of elastic stiffness matrix

The element stiffness matrix is of size 40 x 40 and the manual calculation becomes quite complicated. By considering a plate displacement acted upon by lateral load structure stiffness matrix validation is done. The relation picked up is the bending problem relation which is given in equation 7. The plate considered for validation is a square plate with all sides simply supported. It is subjected to a lateral UDL of magnitude q/unit area. The

plate gets deflected and maximum deflection (W_{max}) [4] will occur at centre and it is made as non-dimensional and is given as,

$$\delta = \frac{W_{max} x D}{q x a^4} \tag{8}$$

where δ = non dimensional deflection, D=flexural rigidity, q=lateral load applied on plate, and a=length of plate.

Table 2: Convergence study of central deflection of isotropic square plate subjected to lateral uniform distributed load simply supported in all sides.

Central deflection exact value ($\delta^{[10]}$)	Mesh size (m × n)	Max. central deflection FEM value (δ)
5*0.00406	2 × 2	0.00189
	4 × 4	0.00401
	6 × 6	0.00405
	8 × 8	0.00406
	10 × 10	0.00406

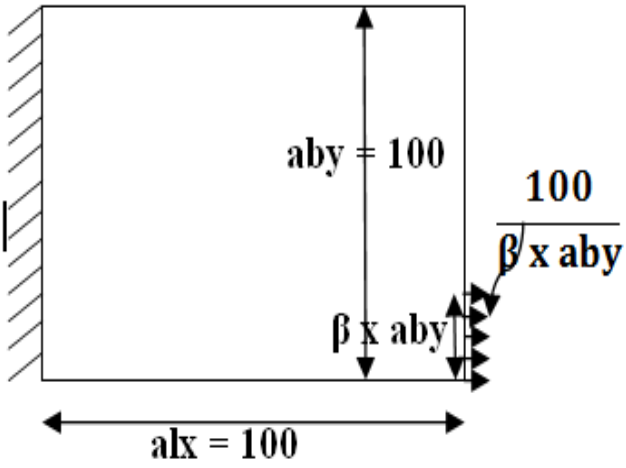

Figure 3: Load application on a cantilever plate of size 100x100.

Table 2 shows convergence study of central deflection of isotropic square plate subjected to lateral uniform distributed load simply supported in all sides. Accurate result is obtained for 10 x 10 meshes and hence, this mesh is used for all analysis. The size of composite plate considered is 100 x 100 and is of unit thickness. The plate is fixed at left side and all other sides are free. A tensile patch load of 100 units is applied at right end in x direction. Patch load is applied from one end of the plate and the width is increased in steps. The contour maps for various patch loads of 0.2, 0.4, 0.6 and 0.8 are obtained only for 2 layered anti-symmetric laminate.
Shown in figures 4-11 are stress contours for σ_1 and σ_2, plotted for 2 layered anti-symmetric composite plate for layers 1 and 2 by varying patch loads from 0.2 to 0.8 with an increase of 0.2, where σ_1 = stress along fibre direction and σ_2 = stress across fibre direction.

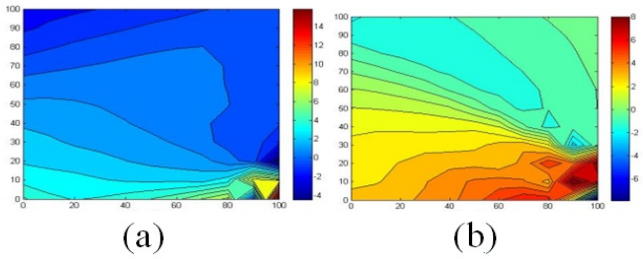

Figure 4: σ_1 distribution for patch load=0.2 for a two layered (30/-30)anti-symmetric composite plate: (a) in layer 1 and (b) in layer 2.

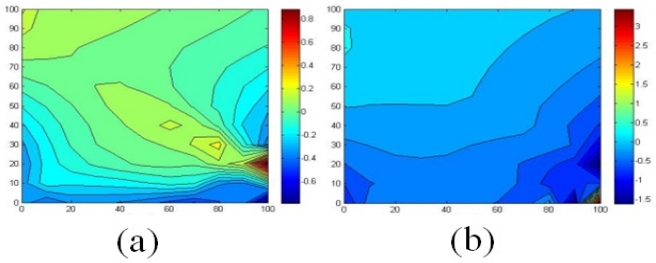

Figure 5: σ_2 distribution for patch load=0.2 for a two layered (30/-30)anti-symmetric composite plate: (a) in layer 1 and (b) in layer 2.

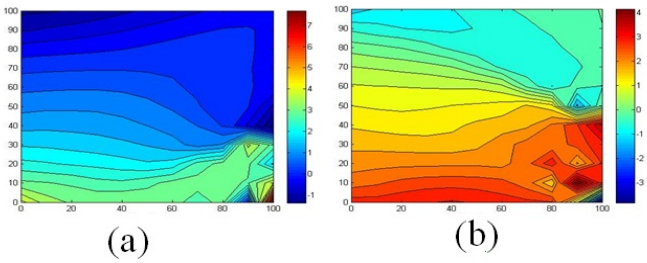

Figure 6: σ_1 distribution for patch load=0.4 for a two layered (30/-30)anti-symmetric composite plate: (a) in layer 1 and (b) in layer 2.

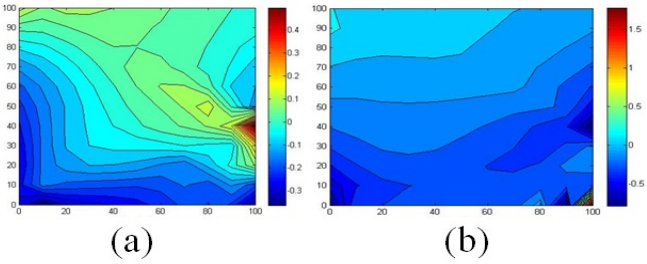

Figure 7: σ_2 distribution for patch load=0.4 for a two layered (30/-30)anti-symmetric composite plate: (a) in layer 1 and (b) in layer 2.

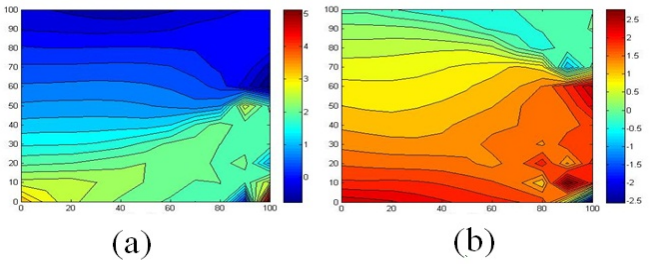

Figure 8: σ_1 distribution for patch load=0.6 for a two layered (30/-30)anti-symmetric composite plate: (a) in layer 1 and (b) in layer 2.

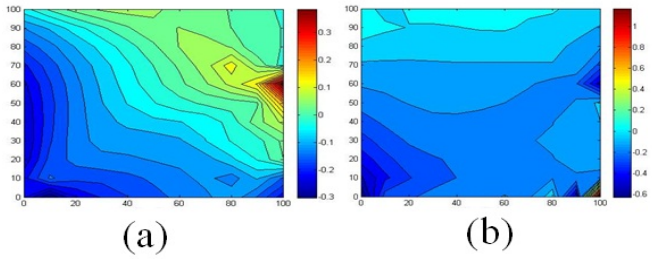

Figure 9: σ_2 distribution for patch load=0.6 for a two layered (30/-30)anti-symmetric composite plate: (a) in layer 1 and (b) in layer 2.

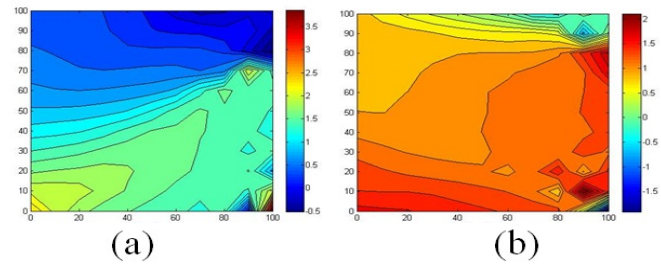

Figure 10: σ_1 distribution for patch load=0.8 for a two layered (30/-30)anti-symmetric composite plate: (a) in layer 1 and (b) in layer 2.

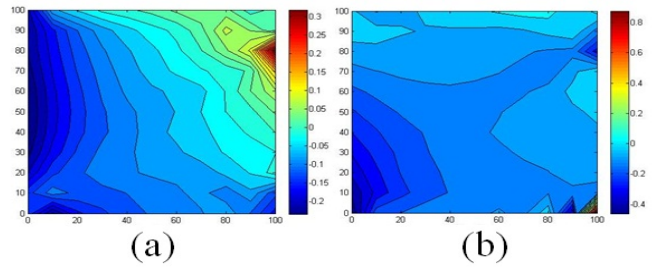

Figure 11: σ_2 distribution for patch load=0.8 for a two layered (30/-30)anti-symmetric composite plate: (a) in layer 1 and (b) in layer 2.

For patch load=0.2, both σ_1 and σ_2 show higher values near the load region. In layer 1, σ_1 changes from tensile to compressive as the distance from the load region increases and the region at top left corner is subjected to high compressive stress. Along fiber direction, tensile stress developed is less in layer 1 as compared to layer 2 whereas maximum compressive stress is in layer 2.

For patch load=0.4, layer 1 and 2 are subjected to compressive stress at the top and tensile stress at bottom in fiber direction. Both σ_1 and σ_2 show higher values near the load region.
In layer 1, σ_1 changes from tensile to compressive as the distance from the load region increases and the region at top left corner is subjected to high compressive stress. Along fiber direction, tensile stress developed is less in layer 1 compared to layer 2 whereas maximum compressive stress is found in layer 2.

For patch load=0.6, major portion of layers are subjected to tensile fiber direction stress as the tensile load is applied for 0.6 times the width from bottom at right end. Stresses developed in layer 1 are more in comparison with layer 2. Stresses across the fiber direction are compressive for major portion of the layer.

For patch load=0.8, major portion of layers are subjected to tensile fiber direction stress as the tensile load is applied for 0.8 times the width from bottom at right end. Stresses developed in layer 1 are more in comparison with layer 2. Stresses across the fiber direction are compressive for major portion of the layer. It is tensile near the end point of location of load.

4 Conclusion

The load deflection phenomena obtained from the coding has been validated with the results obtained from the classical solution. For all cases considered in this work, general fiber direction stresses are tensile near the loading region and compressive in top region. Maximum stresses have been found near the end of the load location. In general, across fiber direction stresses are compressive near loading region and tensile in the region away from load. Stresses across the fiber direction are less in comparison with the stresses along fiber direction. In almost all cases maximum stresses are developed in the corner element near the loading region.

References

[1] S. Tolson and N. Zasaras, "Finite element analysis of progressive failure in laminated composite plates", Computers Structures, vol. 38, pp. 361-376, 1991.

[2] Sharad D. Pawar and Abhay Utpat, "Analysis of composite laminate for maximum stiffness", J. Recent Technology and Engineering, vol. 3, pp. 60-66, 2014.

[3] Sidda Reddy, A. Ramanjaneya Reddy, J. Suresh Kumar K. and Vijaya Kumar Reddy, "Bending analysis of laminated composite plates using finite element method", J. Engineering Science and Technology, vol. 4, pp. 177-190, 2012.

[4] Timoshenko and Woinowsky-Krieger, "Theory of Plates and Shells", McGraw-Hill, New York.

Research Paper

Whispering Gallery Mode Resonators at Optical and Terahertz Frequencies: A Brief Review

Arjun Rao[1*], Cijy Mathai[2], Niraj Joshi[1], A. Jayarama[3], Siddartha Duttagupta[4]

A. V. Gopal[5], S. S. Prabhu[5] and Richard Pinto[1]

[1]E & C Dept.,Sahyadri College of Engineering & Management, Mangalore -575007

[2]Physics Dept., Indian Institute of Technology Bombay, Mumbai-400076

[3]Physics Dept., Sahyadri College of Engineering & Management, Mangalore -575007

[4]Electrical Engineering Dept., Indian Institute of Technology Bombay, Mumbai-400076

[5]Condensed Matter Physics and Material Sciences Dept., Tata Institute of Fundamental Research, Mumbai-400005

*Email: arjunsr92@gmail.com

Abstract

Whispering Gallery Mode Resonators represent a class of cavity devices with exceptional properties such as extremely small mode volume, very high power density, and very narrow spectral line width. Their importance for applications in very sensitive micro-sensors, have been recognized only in recent years. The sensitivity of this resonant technique has been found to be single molecular level, higher than that compared to most optical single-pass devices such as surface plasmon resonance biosensors. In this paper we present a brief review of the field of WGM resonators, which includes the basic concept, the geometrical structures of resonators such as microdiscs, microtoroids and microspheres; the techniques for their fabrication and some of the most important applications as biosensors.

Keywords: WGMR, dielectric, THz, Optical, resonators, biosensor.

1 Introduction

Optical resonators play an important role in modern optics, both as optical filters as well as laser devices. They are also important for nonlinear optics experiments as well as accurate tools for measurements [1-5].

However, bulk optical resonators have certain limitations due to their weight, size, alignment and stability problems. Most of these problems have been overcome by the integrated optics approach. A particular class of resonators, which has emerged in the recent years and has found many applications, is that of integrated ring resonators [6].

In the spectrum of electromagnetic waves, the terahertz range is a narrow window with wavelengths between 3mm and 30m or frequencies between 100 GHz and 10 THz. The THz range, in between infrared and radio waves, has some unique properties. Most of the plastics, textiles, paper and cardboard etc., are transparent to terahertz waves. Further, many biomolecules such as proteins, narcotics and explosives, show characteristic absorption lines - spectral fingerprints - at terahertz frequencies. Further, terahertz waves do not cause any ionizing effect and hence, are generally considered biologically safe. Figure 1 shows the spectrum of electromagnetic waves.

Whispering gallery modes (WGM) are specific resonant modes of a wave field which are confined inside a cavity with polished surfaces due to a series of total internal reflections. From practical considerations, the most interesting Whispering gallery mode resonators (WGMR) are in the optical domain, since they exhibit many unique properties, such as low mode volumes, small sizes of resonators and ultra-high Q-factors [7].

Historically, the phenomenon of whispering gallery waves was first observed by Lord Rayleigh in the 19^{th} century under the dome of St. Paul's cathedral in London. This phenomenon is due to the fact that while propagation of "whiper" or sound waves is directly proportional to the inverse of the square of the distance in normal mode, it is directly proportional to the inverse of the distance in whispering gallery mode. Subsequently, it was realized during the beginning of the 20^{th} century that a phenomena similar to the acoustic whispering gallery waves could exist in the electromagnetic domain. However, the resonator dimensions required in the electromagnetic domain would be much smaller than those of the acoustic whispering gallery waves [7]. But the real study on WGMRs in the optical domain started only in 1990s. This lead to the study of WGMs in THz frequencies, which have an advantage of ease of fabrication of resonators and resonator coupling with the waveguides due to fact that the dimensions involved at THz frequencies are in the millimeter/sub millimeter range unlike the WGMRs in optical domain which are in micrometer range.

Further, the ease of fabrication and capability for on-chip integration of devices, makes WGMRs ideally suited for variety of applications. In this article, some key issues concerning WGMRs which include basic concept of WGMRs, simulation of WGMR at THz frequencies, resonator geometries, coupling of WGMRs with waveguides, resonator performance parameters and important practical applications are discussed.

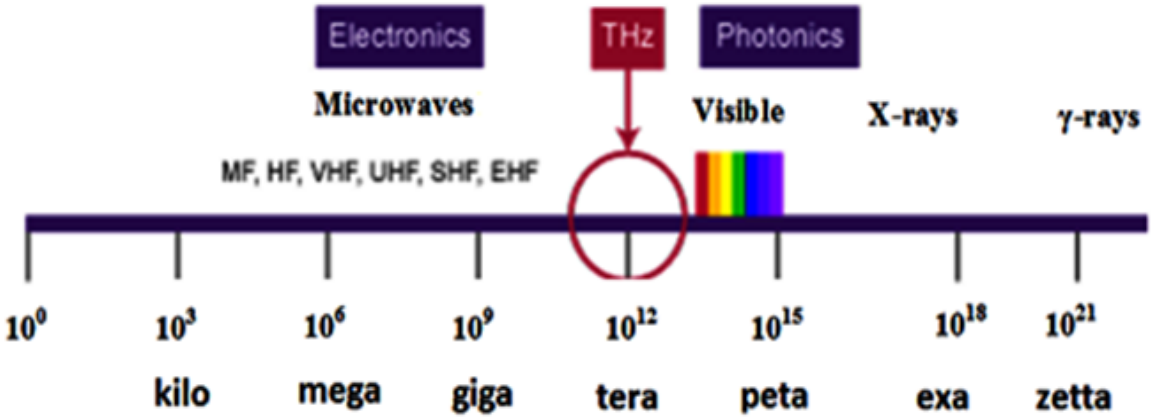

Figure 1: Spectrum of electromagnetic waves.

2 Whispering Gallery Mode Resonator

2.1 Basic Concept

Resonant phenomena in cavities in mechanical, acoustic and optical domains frequently depend on the geometric properties such as size and shape, and also on the composition of the cavities. Such resonances are often known as morphology-dependent resonances (MDRs). An important example of MDR is that of whispering gallery mode resonator in the acoustic domain [8]. As mentioned in the introduction, the WGM in the acoustic domain comprises a moving pressure wave guided around a closed concave surface, like the whispering gallery in St. Paul's Cathedral shown in a schematic Figure 2(a).

From geometric considerations, neglecting absorption, scattering, and material dispersion, these bound modes are guided by repeated total internal reflections and continue endlessly [8]. However, in reality, the wave losses continue through the surface via absorption, scattering, and material dispersion, and the mode undergoes a decay in its amplitude, in the absence of an external excitation [9], thereby causing a finite lifetime. It is important to note that WGM is a subclass of MDR and is characterized by its surface mode nature and high quality (Q) factors as a result of low losses.

Figure 2(b) shows the schematic of WGM in the optical domain illustrating WGMs can also occur in optical cavities having a closed concave interface. Among the most important and simplest WGM geometries in the optical domain are discs/cylinders, spheres, and ring cavities which have been studied extensively during the last two decades. Since the resonators in the optical domain are in the region of few 10's of micrometers, they are generally difficult to fabricate and also tune to the optical waveguide, though they give rise to extremely high Q factors. On the other hand, THz waves have an advantage since the WGMRs in the THz domain are in the sub-millimeter and millimeter range which are easy to fabricate and also to tune to the THz waveguide.

Hence, substantial work is going on currently on WGMRs in the THz domain.

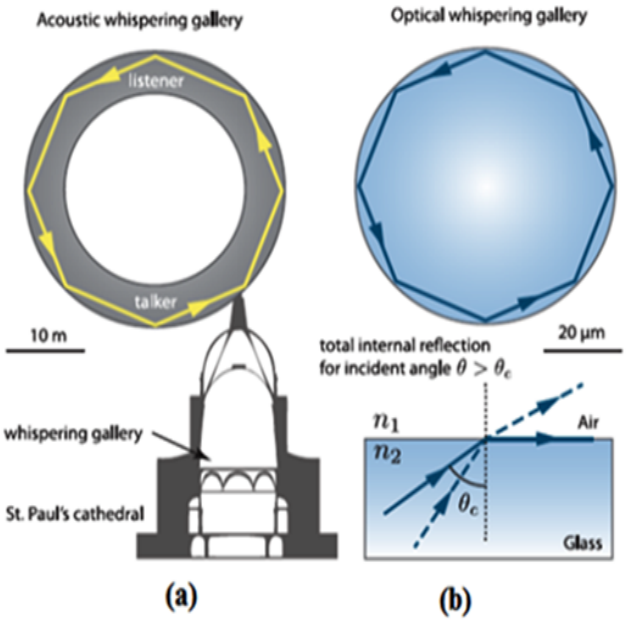

Figure 2: WGMs supported by total internal reflection in (a) an acoustic mode, and (b) an optical wave [10].

2.2 Simulation of WGMR tuned to a THz waveguide

An interesting phenomenon in optical as well as in THz domain for MGRs is that the continuous wave (CW) transmitted light intensity spectrum has several sharp peaks, depending upon the resonant conditions in WGMR, at very stable intervals between two successive peaks. The WGMR used in most cases is a low loss quartz microsphere in the case of optical domain and low loss quartz millimeter size microsphere in THz domain. Further, a minute change in the size of the microsphere or a change in the optical properties of the surrounding medium would shift resonant frequencies. In other words, molecular adsorption on the surface of the microsphere leads to a shift in resonant frequencies due to change in the effective size of the microsphere and/or due to the change in the refractive index of the surrounding medium. Therefore, to detect a specific molecule in extremely small

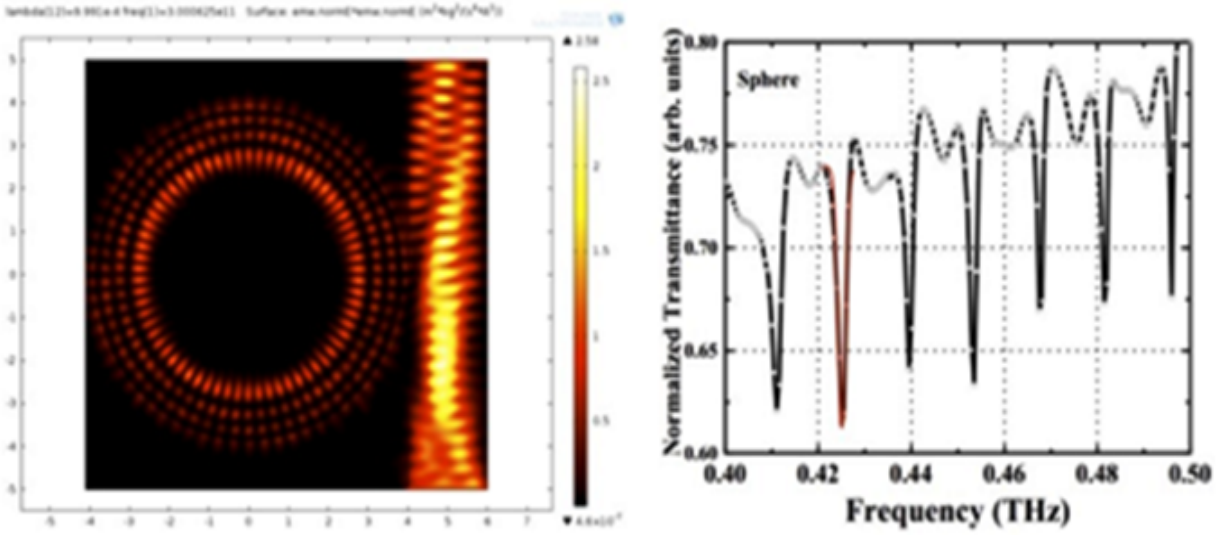

Figure 3: (a) WGMR response in the rectangular waveguide coupling mode. Cavity resonator material: Quartz (n=1.5), Dimension: 5 mm diameter. (b) Transmission spectrum of WGM cavity resonator. Also shown is the theoretical fit Gaussian function for the resonance curve at 0.425 THz [11].

quantities, the WGMR configuration which includes the tunable range of excitation laser, the gap between the microsphere and waveguide, the microsphere size, and the refractive index of the materials, need to be designed and optimized. Since the experimental methods to optimize WGMR parameters are very involved and expensive, an approach to the problem with a simulation model is highly desirable [11].
Shown in Figure 3 is the simulation result obtained with 5 millimeter quartz sphere tuned to a rectangular THz waveguide in the CW-mode. Simulation was carried out using COMSOL Multiphysics vr. 4.4. Figure 3(a) shows WGMR response in the rectangular waveguide coupling mode. Cavity resonator material used is Quartz sphere with refractive index, n=1.5 and 5 mm diameter; Figure 3(b) shows the CW-transmission spectrum of WGM quartz cavity resonator, in which the red peak indicates a theoretical fit Gaussian function for the resonance curve at 0.425 THz [11].

2.3 Quality factor of whispering gallery mode resonator

The most commonly used definition of quality factor is frequency-to-bandwidth ratio of the resonator defined as:

$$Q = \frac{f_r}{\Delta f} = \frac{\omega_r}{\Delta \omega} \tag{1}$$

where f_r is the resonant frequency, Δf is the resonance width or full width at half maximum; here, $\omega_r = 2\pi f_r$ is the angular resonant frequency and $\Delta\omega$ is the angular half-power bandwidth.

Most applications of WGMRs require the realization of very high Q factors. Since its first demonstration in 1987, Q factor of microsphere WGMRs have improved from nearly 10^6 to 10^9 in the red and near-infrared areas of spectrum. It was realized that this Q factor was considerably lower than the limiting losses determined by intrinsic material qualities. It was also observed that in laboratory conditions the Q factor decreases within a short time span primarily due to deposition of micro dust and water vapour under high humidity conditions on the microsphere WGMR surface [12].

The Q factor of WGMR depends on four contributing factors as follows:

(a) Q_{rad} – Q factor due to decay caused by the fact that, unlike a flat surface, the total internal reflection from a curved surface leads to a radiation of the wave from the dielectric sphere. Such decay can be called the radiative decay. Corresponding to this phenomenon we define a radiative quality factor (Q_{rad}).

(b) Q_{ss} – Quality factor due to surface scattering losses due to residual surface irregularities.

(c) Q_{Cont} – Quality factor due to surface contamination.

(d) Q_{mat} – Quality factor due to material property of the resonator; this is related to the contribution due to absorption of light and bulk Rayleigh scattering in the material of the microresonator.

Hence, effective Q factor is

$$Q_{eff}^{-1} = Q_{rad}^{-1} + Q_{ss}^{-1} + Q_{cont}^{-1} + Q_{mat}^{-1} \tag{2}$$

where Q_{rad}^{-1} is due to intrinsic radiative (curvature) losses which vanish exponentially with increasing microsphere diameter D; so with $D/\lambda > 15$, $Q_{rad} > 10^{11}$ (λ is the wavelength); Q_{ss}^{-1} is due to scattering losses on residual surface irregularities which can prevail in intermediate sized microspheres. Q_{ss} can be calculated based on the model of Rayleigh scattering by molecular

sized surface inhomogeneities under grazing incidence and total internal reflection:

$$Q_{ss} = \frac{\lambda^2 D}{2\pi^2 \sigma^2 B} \tag{3}$$

where σ and B are the rms roughness and the correlation length of surface irregularities, respectively. With the numerical values for $\sigma = 0.3$ nm and B = 3 nm reported for glass surfaces, one obtains $Q_{ss}^{-1} << 10^{-10}$ may be expected only in large spheres, D » 100 μm.

Q_{Cont}^{-1} is due to losses introduced by surface contaminants. In the absence of contaminants the Q factor of large spheres would reach the limit obtained by material losses Q_{mat}^{-1} which is due intrinsic optical quality of the material of the microsphere. The principal limit for microsphere Q_{mat} is given by,

$$Q_{mat} = \frac{2\pi n}{\alpha \lambda} \tag{4}$$

where n is refractive index, α is attenuation coefficient and λ is wavelength. The measured Q in microspheres of high-purity fused silica with diameter 500 – 1000 μm fabricated by an oxygen – hydrogen microburner at 633 nm is $\approx 0.9 \times 10^{10}$.

Further, larger Q ($\approx 10^{11}$)can be expected close to the minimum of attenuation at λ=1.55 μm wavelength in fused silica. In order to record Q values for applications it is important to not only fabricate high quality microspheres but also to preserve them in evacuated/dry gas filled chamber. Microspheres also can be preserved to achieve record Q factors by chemical treatment which prevents surface hydration from the atmosphere or by making the surface hydrophobic.

3 WGMR at THz frequencies

3.1 Coupling methods

WGM microsphere cavities are intrinsically high quality resonators and one of the important considerations for applications is the efficiency of light evanescent coupling with the waveguide. Figure 4 shows a schematic of a spherical WGM resonator and the waveguide.

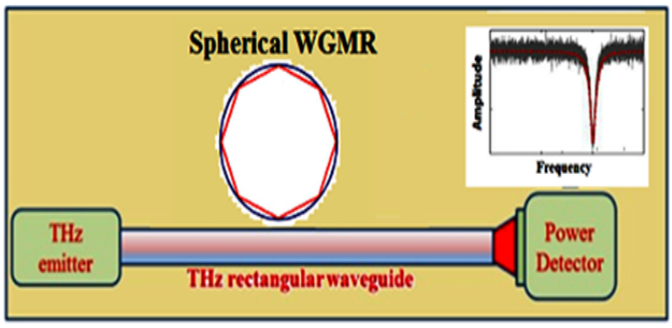

Figure 4: Schematic of a spherical WGM resonator coupled to waveguide (direct waveguide coupling).

WGM optical coupling using propagative free beams is not efficient due to the weak radiative transfer to WGMs which can be seen as quasi-bound state of light trapped inside a dielectric material. Many methods have been developed to overcome this disadvantage. They all rely on energy exchange between a WGM and total internal reflection waves or the evanescent part of guided modes. The prism coupling configuration described in Figure 5(a), based on total internal reflection, is the earliest method used to couple light in WGM microresonators [13-15]. This approach can be implemented using an angle polished optical fiber instead of a prism [16] as shown in Figure 5(b). More recently, tapered fibers have been used to critically couple microsphere high-Q-factor WGM resonators [17-19] as shown in see Figure 5(c).

Using this technique, it is possible to obtain transfer of the incoming power to the microresonator mode [17]. In integrated optics, optical waveguides are used to efficiently couple light inside WGM discs or microspheres [20-22]. The coupling efficiency can be adjusted by controlling the gap between the optical waveguide and the resonator.

3.2 Measurement methods

Primarily two types of measurement techniques can be used to accurately measure high-Q-factor of WGM resonators based on the analysis of the intensity transmission transient profile namely, stationary approach and dynamical approach.

Stationary approach: The most common method used to measure the Q-factors of high and ultra-high-quality WGM microresonators involves linearly scanning of the frequency of a narrow probe laser at the input of the resonator and to simultaneously record its transmission as shown in Figure 4. The frequency of the laser is linearly swept while keeping the amplitude |sin(t)| constant. The source is modeled by as a monochromatic signal whose instantaneous frequency is written as $v(t) = v_i + v_s(t)$, where v_i is the initial frequency and v_i is the frequency sweeping rate. The laser probe is attenuated only when it is tuned to the resonator frequency v_0 (resonant frequency). Experimentally, one can observe, in the time domain, a dip in the transmission spectrum of the resonator as shown in Figure 4. An accurate calibration of v_s allows the frequency spectrum to be measured [12].

Dynamical approach: The Stationary approach is valid only for very low sweeping rates, $v_s << v_{so}$, which is necessary to record the stationary response of the resonator; v_{so} is the scanning rate corresponding to bandwidth of the resonator. For higher-frequency sweeping rates, the excitation cannot be considered as stationary and a ringing phenomenon strongly modifies the profile of the transmission spectrum due to the beating of the input and the intracavity fields [22-24].

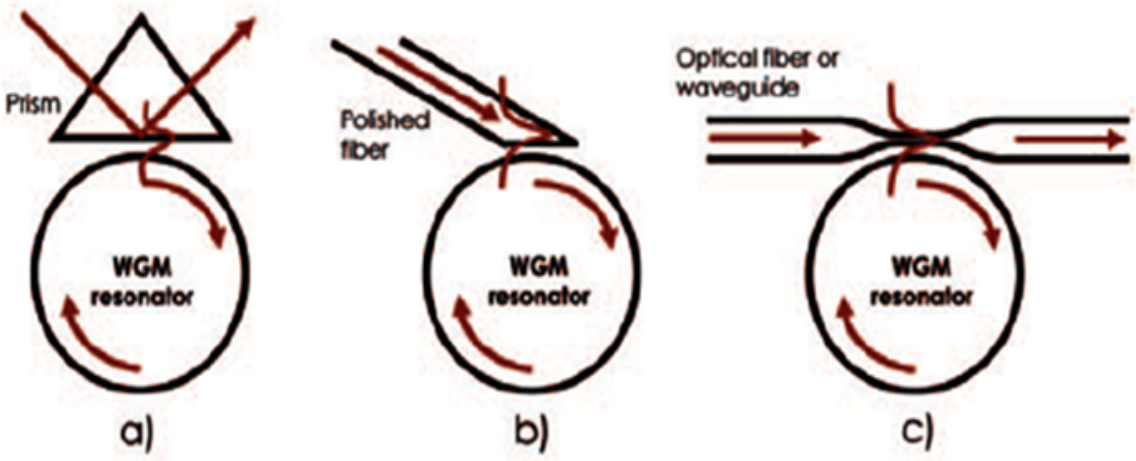

Figure 5: a) Prism coupling using frustrated total internal reflection (kretschmann geometry); b) Slant-cut optical fiber coupling; c) Tapered fiber or optical waveguide coupling [12].

4 Fabrication of WGM micro resonators

As described in above sections, there are many geometries of WGMRs, each of them having advantages and drawbacks. Three major parameters that must be considered in order to assess the usefulness of a given type are: the optical quality of the resonator material, the ease of fabrication and the achievable value of Q-factor. The fabrication techniques of the most common resonating structures are reviewed in this section [12]. Among the resonator materials, glasses, and in particular high purity optical grade silica, are widely used primarily because of the difficulty in fabrication and also the high cost of crystalline materials. Several WGM resonators have been fabricated in the form of ring, sphere, toroid, and elliptical geometries which have been implemented using a wide variety of materials, including glass, silicon, compound semiconductors, silica, and crystalline material. Many methods have been used to fabricate WGMRs with standard semiconductor processing techniques. Ferroelectric resonators can also be used for engineering of the modal spectrum with RF and applied DC fields, since refraction index of the ferroelectric material changes with applied electrical field [12]. It is also interesting to note that, calcium fluoride and magnesium fluoride resonators made with highly transparent crystals, exhibit the highest reported Q factors. A brief review of fabrication methods and the Q factors obtained with cylindrical, disc, toroidal and microspherical WGMRs is presented below.

4.1 Cylindrical

Cylindrical WGMRs have the simplest geometry and are easy to fabricate. However, they have the drawback that, due to the longitudinal degree of freedom in such a structure, a coupled beam in this case, as compared to the microsphere, spreads along the cylinder length and eventually vanishes. This happens even if there is no material loss [12]. One of the earliest experiments designed to show, that spiral whispering mode propagation occurs in closed optical structures of circular cross section, was carried out using cylinders machined from polymethyl methacrylate [25]. The simplest cylindrical WGMR, however, is fabricated with a small piece of a conventional telecom single-mode optical fiber (chosen due to its high material quality), prepared by suitably stripping the cladding and coating [26, 27]. In this case, too, an experimental analysis has shown that if the fiber is tilted i.e. not exactly perpendicular to the in-coupled optical beam, then "spiral" WGMs, tracing a helical path along the fiber, are triggered. Hence, WGMR cylindrical geometries are generally not preferred [28].

4.2 Microdiscs and Toroids

Some of the early solid-state lasers were among the first devices effectively exploiting WGM light confinement [29, 30]. Walsh (1963) et al., have reported pulsed laser operation at room temperature by exploiting total internal reflection in a ruby ring. One of their ring lasers had internal diameter 22.2 mm, external diameter 23.8 mm, and height 3.18 mm; the other one 14.3 mm 15.9 mm, and 3.2 mm respectively. The c-axis was perpendicular to the plane of both rings, and concentration was 0.05% by weight. The rings were fabricated and mechanically polished; all surfaces except the inside diameter surface were optically polished. The authors estimated that the Q-value of these cavities was between 10^8 and 10^9, and noted that these values were about two orders of magnitude larger than those measured in silvered rods [30]. In the same year, Ross et. al. fabricated two lasers in cylindrical toroids of ruby, the material being a 0.035% ruby of medium quality, with c-axis oriented at 90° to toroid axis. The size of these compact lasers was 13mm outer diameter, 9mm or 11mm inner diameter, 5mm height. They reported the outstanding property of this approach which made it possible to combine an extremely high resonator Q with a moderate mode selection which led to quasi-continuous oscillations in an inhomogeneous material like ruby [29].

All these millimeter-sized resonators were produced by

mechanical polishing followed by thermal annealing. The JPL group [31], has developed a fabrication technique which is based on computer controled precision lathe, followed by a conventional polishing technique. By using the diamond turning process they were also able to realize a special single-mode cavity, formed by a small 5 μm $\times$ 3 μm waveguide on top of a cylinder [32].

In a very recent paper [33], a similar procedure was used to fabricate high-Q lithium niobate discs and spheroids made from Z-cut lithium niobate wafers. The polishing procedure of crystalline discs was in this case optimized by using a lapping machine. The almost spherical profile was obtained through a rotational stage whose pivot point could be finely adjusted followed by elaborate polishing and cleaning steps. In this way they achieved an intrinsic disc Q-factor of 1.3×10^8.

Both microdiscs and microspheres by virtue of their being discrete objects make them difficult to be coupled to optical integrated circuits. Further, optical polishing cannot be easily adapted to sub-mm devices. In this context, for the development of micron-sized robust integrated devices a much more effective approach is the one first proposed by Vahala's group [34] who demonstrated a method for fabricating toroid-shaped silica microresonators-on-a-chip with Q values in excess of 10^8. Figure 6 shows a scanning electron micrograph of a silica microdisc, fabricated on silicon wafers prepared with a 2 μm layer of silicon dioxide.

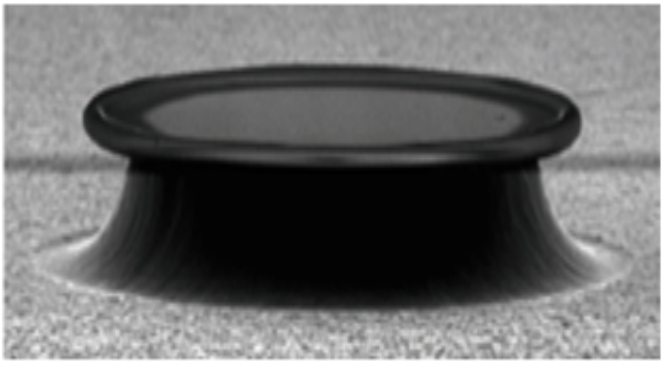

Figure 6: SEM image of a silica microdisc [36].

The fabrication process for the torroid microresonator composed of four steps as follows: photolithography to create disc-shaped photo-resist pads typically 160 μm diameter; pattern transfer into the SiO_2 layer; selective dry etch followed by selective reflow of the patterned silica. They demonstrated a chip-based monolithic microcavity Raman laser, exhibiting high efficiency, ultralow threshold, and single-mode emission. For a microtoroid with diameter $\approx$ 61μm and thickness $\approx$ 3.7μm they measured a quality factor and a threshold power at 1550 nm $\approx$ 74 μW for Raman lasing near 1680nm [35].

In another experiment, stimulated emission was achieved by incorporating erbium ions into the toroidal microcavity; this was realised by a group in Grenoble [37], that developed a process for the integration of silicon-rich oxide (SRO) layers doped with Er into toroidal microcavities. The SRO:Er thin film was obtained in a high vacuum vessel by coevaporation under N atmosphere of silicon monoxide and erbium. Each sample was annealed under forming gas (95% - 5%) to activate emitters. First, silica microdiscs on circular silicon pillars were fabricated by defining the discs in photoresist by optical lithography and transferring them to the silica or SRO layer by chemical etching using buffered HF; arrays of silica microdiscs on silicon pillars were obtained by etching the silicon substrate by SF_6/Ar reactive ion etching. In a second step, CO_2 laser was used for selective reflow treatment to form the toroidal microcavities, by taking advantage of the much larger (100:1) thermal conductivity of silicon than silica. During reflow treatment, only the silica layer is heated, cooling the centre of the silica microdisc and the silicon pillar acts as a heat-sink. This results in a selective melting and smoothing of the edge of the silica disc, without affecting its centre. It was noted that the final surface roughness of a toroidal microcavity produced is close to that of a liquid droplet, as can be seen in the micrograph of Figure 7.

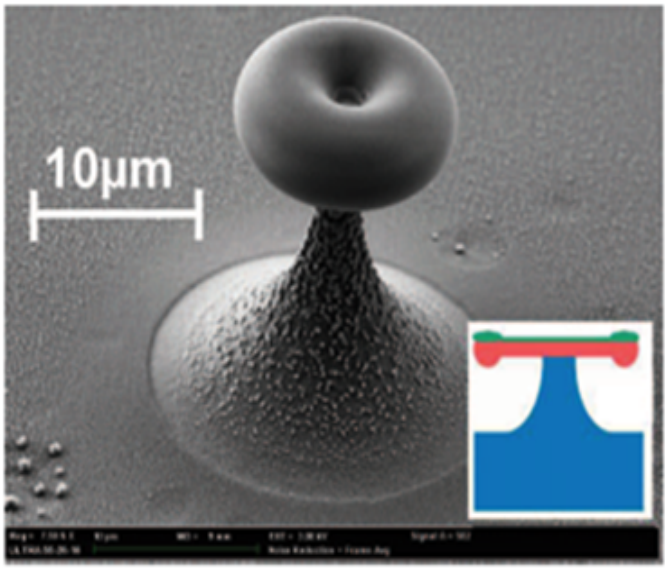

Figure 7: Scanning electron micrograph of a toroidal microresonator of diameter 13 μm after selective reflow. An SRO:Er layer 200nm thick had previously been deposited on top of a 2.7 μm silica layer [37].

4.3 Spherical

One of the main important advantages of microspheres is that they can be fabricated in the laboratory from a variety of inorganic and organic materials. Liquid microdroplets or microspheres have been studied since the very beginning of this field. In recent years, polymer microspheres and their dispersions have been widely used in photonics as well as in medical and biochemical applications [38]. Polymer microspheres can be fabricated both by chemical methods such as heterogeneous polymerization and by physical methods, like emulsification, coacervation and spray-drying [12]. One important route is to fabricate first a PMMA fiber

followed by fabrication of a microsphere by melting the tip of the fiber, just as in the case of silica microspheres. The Q-factor of the microspheres was found to be rather low ($\approx 5 \times 10^4$) [39], most likely due to impurities in the material and surface inhomogeneities caused by uneven heating. Later, the same authors [39], improved the Q-factor up to 10^6 by removing the impurities in the polymer. Microspheres were prepared by placing a controlled drop of the purified PMMA using a microsyringe at the tip of a PMMA fiber. Hollow PMMA spheres could also be obtained by injecting a certain amount of air into the liquid polymer before depositing it onto the fiber tip. Using another approach Li et al.[40], fabricated dye molecule-doped microspheres in a microfluidic channel, which can also create arrays onto a chip.

Fabrication of glass microspheres can be carried out using variety of techniques. One technique is based on the melting of glass powder in the furnace and dropping the viscous glass onto a spinning plate [12]. A process, used for a multi-component fluoride glass (ZrF_4) is based on melting the raw materials at 1000°C inside an induction furnace; the molten material is poured in a fine stream into liquid N_2 followed by collection of spherical particles which passed through a filter [41]. One problem in this technique is the easy contamination of the sphere surface. Hence, chemical polishing in chemicals like $ZrOCl_2 - 8H_2O$ is required. Another approach involves the use of magnetic levitation to keep the glass sample suspended while heated. Here, a glass cube, located in a platinum cage at the edge of the inner magnet, is made to levitate while melting by the effect of a focused CO_2 laser beam; glass microspheres were obtained after cooling [42, 43]. Subsequent polishing to optical grade improves the quality of the spheres. Another method to produce glass microspheres made use of a rotating electric arc. Microspheres with diameters between 2 and 24 μm were fabricated by processing of the glass powder; 85% of particles were transformed into microspheres [44]. One disadvantage of these techniques is however, is that one obtains a number of free spheres with a rather large size distribution which are difficult to be controlled [12]. The selected spheres can be picked up with an evacuated glass capillary for further use as a WGMR.

Another simple and effective method to produce micro spheres with the desired diameter is based on the melting of the tip of a glass fiber using different heating sources, such as high-power CO_2 laser and electric arc etc. [45, 46]. With heating the distal tip of a fiber, the glass reflows to form a spherical volume due to surface tension. Because of high viscosity of silica, the reflowed structure becomes highly spherical and extremely uniform with eccentricities as low as 1–2%. Further, the spherical surface has low intrinsic roughness, as low as 1 nm r.m.s, thereby causing very small surface scattering losses. A typical silica microsphere obtained in this way is shown in Figure 8(b). The light coupling in the tapered fiber can be seen in the background (out of focus). The operation of the resonator is not affected by the presence of the stem due to negligible overlap with the perturbation region, since the excited optical modes typically lie in the equatorial plane; on the other hand, it helps easy handling of the microsphere. Reproducible spherical diameters were obtained with the size of the spheres increasing with increasing number of electric arc shots, till the diameter saturated at about 350 m in the case of standard 125 μm singlemode optical fibers. Figure 8(a) shows the growth of the sphere diameter with the number of shots; the picture of a typical 250 μm microsphere is shown in figure 8(b). This technique allows one to fabricate microspheres with diameters in the range d to 2d, where d is the outer diameter of the uncoated fiber. Spheres, from 20 to 100 μm range can be obtained by tapering the fiber. The minimum diameter obtained was 40 μm using tapered fibers [47].

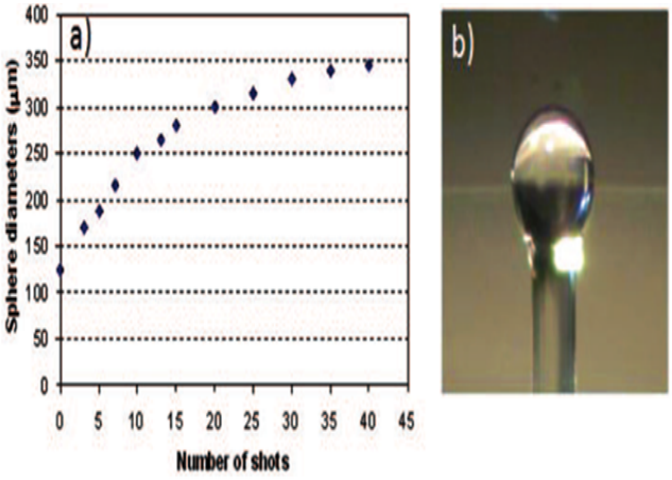

Figure 8: a) Size of the microspheres prepared at the tip of a 125 μm telecom fiber, as a function of the arc shots. b) Optical image of a microsphere with 250 μm diameter [47].

5 Applications

WGMRs exhibit unique properties in the field of sensing. The main advantage of a WGMR sensor is due to the fact that, the trapped photons are able to circulate on their orbit several times before exiting the WGMR if scattering losses by total internal reflection at the boundary of the resonator are low and absorption of light in the material is extremely low. In this section we present one particular field of sensor applications viz biosensing by microspherical WGMRs, where rapid progress has been achieved during the last few years.

The sensing mechanism is based on the fact that, when a nano or microscopic object (like a molecule or a bacterium) is brought in proximity with the confined circulating light, the interaction is resonantly reinforced due to the reactive mechanism. A change in the Q-factor of the WGMR or a shift in the resonance frequency is caused due to the change in radius and/or refractive index of the surface of the sphere, through the interaction of the evanescent part of the WGM field. In principle, the sensitivity can be very high such that it can detect single molecules or single nanoparticles.

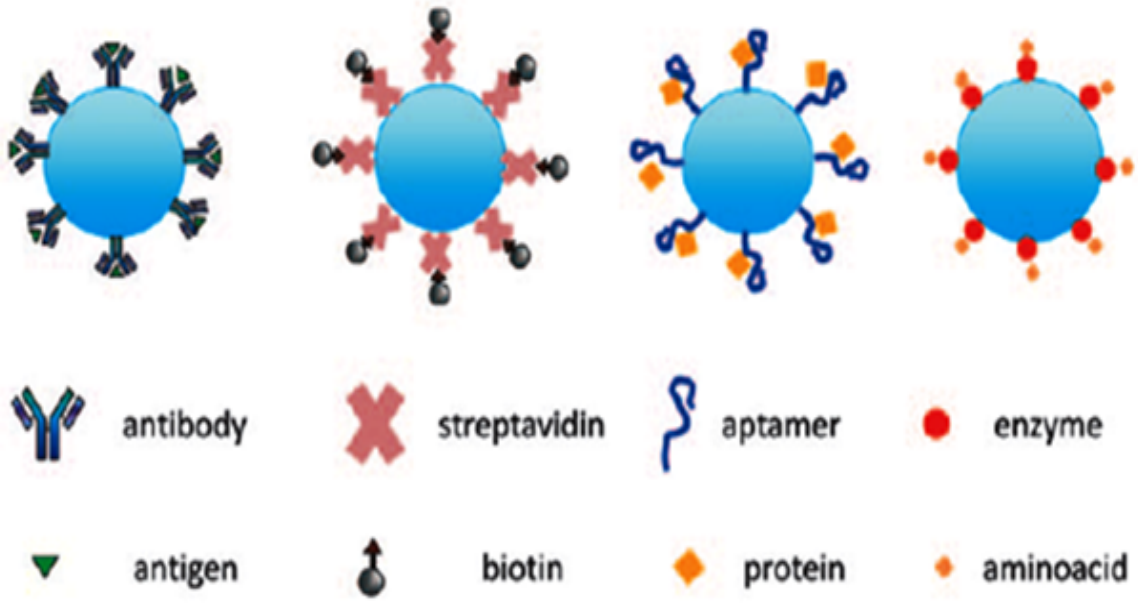

Figure 9: Schematic of a WGM biosensor, resulting from the combination of a WGMR with a sensing layer. Middle row: main ligands or receptors. Bottom: main analytes [12].

The characteristics of a WGM miniature biosensor based on fiber-microsphere coupling have been studied numerically [48]. The authors have solved time-domain Maxwell's equations to obtain electromagnetic and radiation fields. They found a down-shift in the microsphere WGM resonance frequency due to an increase of either the refractive index of the surrounding medium or the effective microsphere size. The larger the change, the stronger the shift is. They also found a linear relationship between effective diameter of the microsphere and the resonance frequency shift.

It has been estimated by simulation [49] that for an optical instrument with ≈ 1 MHz resolution, a sensitivity of the WGMR biosensor as good as ≈ 0.1 nm for the detection of attachment/adsorption of molecules on the microsphere and as good as $\approx 10^{-3}$ for the detection of refractive index change in the surrounding medium is achievable. Such high sensitivities of WGM miniature biosensors are extremely important in applications such as drug discovery, protein identification, peptide monitoring, DNA detection, etc. The important characteristics of a WGMR based biosensor are sensitivity, selectivity, reversibility and stability. The biochemical receptors such as antibody, antigen, DNA, enzyme and aptamer mainly provide for the selectivity as well as stability and reversibility of the WGM biosensor. The sensitivity is primarily being provided by the quality of the optical platform.

A schematic of a biosensor based on WGM resonators, after the functionalization, interfaced with the biological recognition element is shown in Figure 9. A schematic of the generally used biological recognition elements: antibody, streptavidin, aptamer and enzyme is shown in middle row in Figure 9; the bottom row in Figure 9 shows the corresponding analytes: antigen, biotin, proteins, and amino acids. The sensors based on antibody are known as immunosensors while aptamer-based sensors are called aptasensors. The antibody shows high specificity and affinity towards the antigen, as indicated by their molecular complementarities. Enzymes are specific in both the substrate they recognize and the reaction they catalyze; Their activities are also regulated by other molecules.

The first experiment that showed the quantitative use of spherical WGMR microsensors in biomedicine dates back to 2002 [50]. Specific detection of proteins was proven in this paper. Further, the same group demonstrated single nucleotide polymorphism analysis by hybridization and the feasibility of multiplexed DNA quantification. An unprecedented sensitivity of 6 pg/mm^2 was demonstrated. By using two microspheres, specific and multiplexed DNA detection was performed, leading to discriminate a single nucleotide mismatch. This technique can be of immense use in detection of gene mutation involved in cancer growth without target labeling.

6 Summary

Light Confinement into small volumes has become an essential requirement for photonic devices. Examples of this are integrated optical circuits, optical fibers, and semiconductor lasers. Whispering Gallery Mode Resonators represent another class of cavity devices with exceptional properties such as very high power density, extremely small mode volume, and very narrow spectral line width. Optical dielectric resonators based on WGMRs are now known since more than three decades. However, their importance for applications in very sensitive microsensors, have been recognized only in recent years. A brief review of the field of WGM resonators, which includes basic concept, the geometrical structures of resonators such as microdiscs, microtoroids

and microspheres; the techniques for their fabrication and some of the most important applications as biosensors are described here.

References

[1] D. Hall and P. Jackson, "The Physics and Technology of Laser Resonators", Taylor and Francis, 1989.

[2] V. Bykov and O. Silichev, "Laser Resonators", Cambridge Intl. Science Publ., 1995.

[3] A. Kudryashov and H. Weber, "Laser Resonators: Novel Design and Development", SPIE Press, 1999.

[4] N. Hodgson and H. Weber, "Laser Resonators and Beam Propagation, 2nd edition", Springer, 2005.

[5] S. K. Dixit, "Filtering Resonators", Nova Science Publishers, 2001.

[6] D. G. Rabus, "Integrated Ring Resonators: The Compendium", Springer, 2007.

[7] Matjaž Gomilšek, "Whispering gallery modes", Ljubljana, Seminar Report, November 2011.

[8] R. Matthew Foreman, D. Jon Swaim and Frank Vollmer, "Whispering gallery mode sensors", Max Planck Institute for the Science of Light, Germany, May 2015.

[9] B. R. Johnson, "Theory of morphology-dependent resonances: shape resonances and width formulas," J. Opt. Soc. Am. A, vol. 10, pp. 343–352, 1993.

[10] F. Vollmer and S. Roy, "Optical resonator based biomolecular sensors and logic devices," J. Indian Inst. Sci., vol. 92, pp. 233–251, 2012.

[11] C. Mathai, S. Prabhu, A. Venugopal, N. Joshi, R. Pinto and S. P. Duttagupta, "Tunable whispering gallery mode cavity in THz frequency domain for sensing applications", unpublished.

[12] G. C. Righini, Y.Dumeige, P. F'eron, M. Ferrari, G. Nunzi Conti, D. Ristic and S. Soria, "Whispering gallery mode microresonators: Fundamentals and applications", vol. 34, 2011.

[13] V. Braginsky, M. Gorodetsky and V. Ilchenko, Phys. Lett. A, vol. 137, pp. 393, 1989.

[14] M. L. Gorodetsky and V. S. Ilchenko, J. Opt. Soc. Am. B, vol. 16, pp. 147, 1999.

[15] F. Treussart, V. Ilchenko, J. Roch, J. Hare, V. Lef'evre-Seguin, J. M. Raimond and S. Haroche, Eur. Phys. J. D, vol. 1, pp. 235, 1998.

[16] V. S. Ilchenko, X. S. Yao and L. Maleki, Opt. Lett., vol. 24, pp. 723, 1999.

[17] M. Cai, O. Painter and K. Vahala, Phys. Rev. Lett., vol. 85, pp. 74, 2000.

[18] V. S. Ilchenko, X. S. Yao and L. Maleki, Opt. Lett., vol. 24, pp. 723, 1999.

[19] J. C. Knight, G. Cheung, F. Jacques and T. A. Birks, Opt. Lett., vol. 22, pp. 1129, 1997.

[20] Y. Panitchob, G. S. Murugan, M. N. Zervas, P. Horak, S. Berneschi, S. Pelli, G. Nunzi Conti and J. S. Wilkinson, Opt. Express, vol. 16, pp. 11066, 2008.

[21] G. Nunzi Conti, S. Berneschi, F. Cosi, S. Pelli, S. Soria, G. C. Righini, M. Dispenza and A. Secchi, Opt. Express, vol. 19, pp. 3651, 2011.

[22] A. A. Savchenkov, A. B. Matsko, V. S. Ilchenko and L. Maleki, Opt. Express, vol. 15, pp. 6768, 2007.

[23] Z. Ioannidis, P. Radmore and I. Giles, Opt. Lett., vol. 13, pp. 422, 1988.

[24] J. Poirson, F. Bretenaker, M. Vallet and A. L. Floch, J. Opt. Soc. Am. B, vol. 14, pp. 2811, 1997.

[25] F. G. Reick, Appl. Opt., vol. 4, pp. 1396, 1965.

[26] T. A. Birks, J. C. Knight and T. E. Dimmick, IEEE Phot. Techn. Lett., vol. 12, pp. 182, 2000.

[27] M. Sumetsky and Y. Dulashko, OSA Proc. OFC-2006, 2006.

[28] A. W. Poon, R. K. Chang and J. A. Lock, Opt. Lett., vol. 23, pp. 1105, 1998.

[29] D. Ross, Proc. IEEE, vol. 51, pp. 468, 1963.

[30] P. Walsh and G. Kemeny, J. Appl. Phys., vol. 34, pp. 956, 1963.

[31] I. S. Grudinin and L. Maleki, Opt. Lett., vol. 32, pp. 166, 2007.

[32] I. Grudinin and L. Maleki, J. Opt. Soc. Am. B, vol. 25, pp. 594, 2008.

[33] G. Nunzi Conti, S. Berneschi, F. Cosi, S. Pelli, S. Soria, G. C. Righini and M. Dispenza, Opt. Express, vol. 19, pp. 3651, 2011.

[34] D. K. Armani, T. J. Kippenberg, S. M. Spillane and K. J. Vahala, Nature, vol. 421, pp. 925, 2003.

[35] T. Kippenberg, S. Spillane, D. Armani and K. J. V., Opt. Lett., vol. 29, pp. 1224, 2004.

[36] D. K. Armani, T. J. Kippenberg, S. M. Spillane and K. J. Vahala, Nature, vol. 421, pp. 925, 2003.

[37] J. B. Jager, P. Noe, E. Picard, V. Calvo, E. Delamadeleine and E. Hadji, Physica E, vol. 41, pp. 1127, 2009.

[38] V. T. Tran, J. P. Benoit and M. C. Venier Julienne, Int. J. Pharmaceut., vol. 407, pp. 1, 2011.

[39] T. Ioppolo, M. Kozhevnikov, V. Stepaniuk and V. Sheverev, Appl. Opt., vol. 47, pp. 3009, 2008.

[40] J. B. Jager, P. Noe, E. Picard, V. Calvo, E. Delamadeleine and E. Hadji, Physica E, vol. 41, pp. 1127, 2009.

[41] K. Miura, K. Tanaka and K. Hirao, J. Non Cryst. Solids, vol. 276, pp. 213-214, 1997.

[42] N. Kitamura, M. Makihara, M. Hamai, T. Sato, I. Mogi, S. Awaji, K. Watanabe and M. Motokawa, Jpn. J. Appl. Phys., vol. L324, pp. 39, 2000.

[43] N. Kitamura, M. Makihara, T. Sato, M. Hamai, I. Mogi, S. Awaji, K. Watanabe and M. Motokawa, J. Non-Cryst. Solids, vol. 624, pp. 293-295, 2001.

[44] I. Bica, Mater. Sci. Engin. B, vol. 77, pp. 210, 2000.

[45] L. Collot, V. Lefevre-Seguin, B. Brune, J. Raimond and S. Haroche, Europhys. Lett., vol. 23, pp. 327, 1992.

[46] C. H. Dong, L. He, Y. F. Xiao, V. Gaddam, S. Ozdemir, H. C. Guo and L. Yang, Appl. Phys. Lett., vol. 94, pp. 231119, 2009.

[47] M. Brenci, R. Calzolai, F. Cosi, G. Nunzi Conti, S. Pelli and G. C. Righini, Proc. SPIE, vol. 6158, pp. 61580, 2006.

[48] S. Arnold, S. Shopova and S. Holler, Opt. Express, vol. 18, pp. 281, 2010.

[49] S. Boriskina and L. Dal Negro, Opt. Lett., vol. 35, pp. 2496, 2005.

[50] F. Vollmer, D. Braun, A. Libchaber, M. Khoshsima, I. Teraoka and S. Arnold, Appl. Phys. Lett., vol. 80, pp. 4057, 2002.

Research Paper

Effects of Corrugation Profile on the Heat Transfer Rate of Fins

Ravichandra Rangappa[1*], G. Vikas[1] and Walid Abdullah Al-suraihi[2]
[1]Mechanical Engineering Dept., Sahyadri College of Engineering & Management, Adyar, Mangalore-575007
[2]Nilai University, Nilai, Negeri Sembilan, Malaysia
*Email: ravichandra.mech@sahyadri.edu.in

Abstract

Heat is a form of energy that can be transformed from one form to another. Practically, heat transfer can exist only when there is a temperature gradient between two substances. The heat transfer phenomenon takes place in three modes, conduction in solids, convection in fluids and radiation through any medium that permits radiation to pass. Fins are used in many kinds of applications to increase the rate of heat transfer from surface area and to provide cooling effects. The fin material has a high thermal conductivity. Heat transfer from the surface of the fin to the surrounding atmosphere is mainly due to convection. Corrugated profiles are very important for convective heat transfer in many engineering applications. Studies and investigations on convective heat transfer in corrugated channels have been carried out using water or air as a working fluid. In this project, the impact of corrugated fin on heat transfer performance is considered as the topic of study. Angular fin is compared with flat fin. Computational simulations were carried out using ANSYS 14.0 FLUENT software and for experimental section, it was done using Heat Transfer Convection Trainer (Model: TERA-CT-115). Both experimental and simulation results revealed the improved heat dissipation in the corrugated fins compared to the flat fins.

Keywords:-Heat dissipation, fin, corrugated shape.

1 Introduction

Heat is defined as energy in travel due to temperature difference. Heat transfer is amongst the most ubiquitous processes in nature. It is even an inevitable process within virtually all machines, devices and instruments. With such a wide scope of application, heat transfer turns into a key part of engineering knowledge base. Heat exchanger is defined as a device permitting the transfer of thermal energy between solid particulates and a fluid, two or more fluids, a fluid and a solid surface at diverse temperatures and thermal contacts. Heat exchangers are not merely used in the procedures for air-conditioning, cryogenic, alternative fuel, refrigeration, petroleum, power heat recovery, nor manufacturing industries. It is also a key function in market availability of many industrial products [1].

A fin material should have a high thermal conductivity; while having a large surface area, fins could carry the heat developed in the application to be carried to the fin surface. Fins exposed to surrounding fluids promote higher convective heat transfer.

A large number of engineering applications use fins to increase the heat transfer rate such as single-double cylinder IC engines, radiators in cars, air-conditioning equipment, refrigerators and CPU heat sinks in the computers. The larger the surface area the greater is the amount of heat transferred. Hence, fins and corrugated profiles are high-efficiency heat transfer structures.

According to Newton's Law of cooling, the heat transfer rate is given by the equation

$$q = hA\,(T_s - T_f) \tag{1}$$

Where, q is the heat transfer rate in W, h is the convection heat transfer coefficient in W/m^2K, A is the surface area through which convection heat transfer takes place in m^2, T_3 is the surface temperature, and T_f is the temperature of the fluid sufficiently far from the surface in K[2].

Above equation 1 states that the heat transfer rate is mainly dependent on the heat transfer coefficient (h) and surface area (A). In order to increase the heat transfer rate, it is obvious to increase either surface area A or heat transfer coefficient h. To Increase h, it would require a high capacity pump or blower because h is a function of coolant velocity. Installing a high capacity pump or blower would be an expensive option. Another way to increase the heat transfer is to increase the surface area of the fins.

Corrugated plate fins have a larger heat transfer surface area and increased turbulence level due to the corrugations. Jogi et al have analyzed the corrugated plate heat exchanger experimentally. Based on their experimental data they proposed a simplified Nusselt number correlation incorporating effects of Reynolds number, Prandtl number, viscosity variation and chevron angle(β) [3]. Tisekar et al have analyzed the performance of corrugated plate heat exchanger with water as a working fluid. It has been found that corrugated plate type is much more efficient than tube type heat exchanger [4]. Khoshvaght et al has studied the thermal-hydraulic characteristics of plate-fin heat exchangers with corrugated/ vortex- generator plate-fin (CVGPF). In this work a new design of the plate fin of corrugated and vortex has been designed. Further, the hydraulic performances of all plate-fins improved as the mass fraction of ethylene glycol in the working fluid increases [5]. Zhao-gang et al have done the parametric study

on the performance of a heat exchanger with corrugated louvered fins. The results have shown that flow depth, fin thickness and ratio of fin pitch and the number of the louvers are the main factors that influence significantly the thermal-hydraulic performance of the heat exchanger with corrugated louvered fins [6]. Kijung et al have reported about heat transfer and fluid flow correlations to describe the performance of heat exchangers that use corrugated louvered fins [7]. They have studied the parameters and optimization procedures to improve the performance of a corrugated louvered fin. In this work it has been found that the fin pitch, louver angle and louver pitch are the three important parameters which affect the performance of the corrugated fins [8]. Jang et al have analyzed the heat transfer and pressure drop characteristics of a primary surface heat exchanger (PSHE) with corrugated fins. Experimental results show that Nusselt number and friction factor correlations were suggested for a PSHE with corrugated surfaces [9].

Use of fins to increase convection heat transfer in an extensive engineering application; and increase the heat transfer rate from the surface area without increasing overall size of the application is a challenging issue. It is observed that heat transfer rate increases with perforations as compared to fins of similar dimensions without perforations. It is noted that in case of triangular perforations optimum higher heat transfer is achieved [10].

This paper gives a detailed comparative study on heat dissipation between a flat fin and a triangular corrugated fin. Both computational and experimental methods were applied to carry out the study.

2 Experimental

The general aim of this work is to analyze the effect of corrugated fins on heat transfer. The specific objectives are:

a. To study the effect of corrugated profile on heat transfer rate.

b. To design and develop a numerical model to analyze the corrugated fins.

c. To develop an experimental setup to study the effect of corrugated fins on heat transfer.

The simulation and experimental work has been carried out for flat and triangular corrugated fins. Design part of the fins was carried by Solid works 3D modelling software. Further, the 3D models were transferred to ANSYS meshing tool to generate the mesh. Heat transfer simulations were set up using FLUENT as solver. Along with the simulations, real fins were fabricated for the same dimensions. Then the fins were tested for heat dissipation using Heat Convection Trainer experimental machine.

2.1 Simulation Setup

The geometry of the fins was developed using Solidworks software. Each designed model contains three fins, with specific fin shape. As per the design, inside the same working domain, triangular corrugated fin has larger surface area than the flat fin. Air was let to flow over the fins from inlet to outlet of working boundary domain as shown in Figures 1 and 2. ANSYS-14 Meshing tool was used to generate the mesh and ANSYS-14 Fluent codes were used as CFD simulation tool. Figures 3 and 4 show the schematics of flat pins-3D and corrugated fins-3D, respectively.

Since accuracy of the simulation largely depends on the quality of mesh, care was taken while generating the mesh. Number of nodes for Flat fin were 40974 and for Triangular corrugated fins were 45180. The elements are 202065 for Flat fins and 225884 for Angular corrugated fins. Figures 5 and 6 illustrate the mesh for both flat and corrugated fins, respectively.

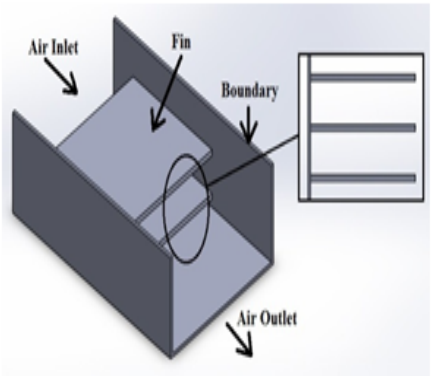

Figure 1: Schematic of Flat Fins-3D.

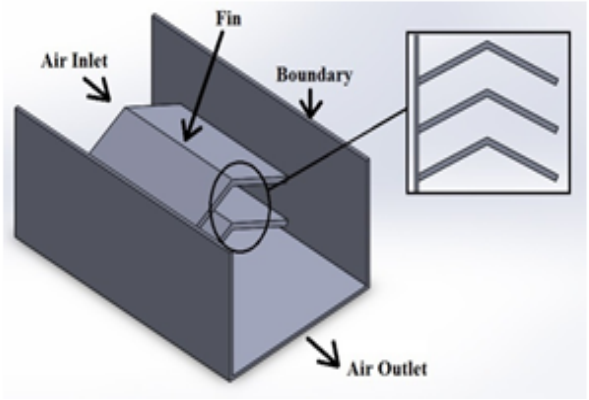

Figure 2: Schematic of Angular Corrugated Fins-3D.

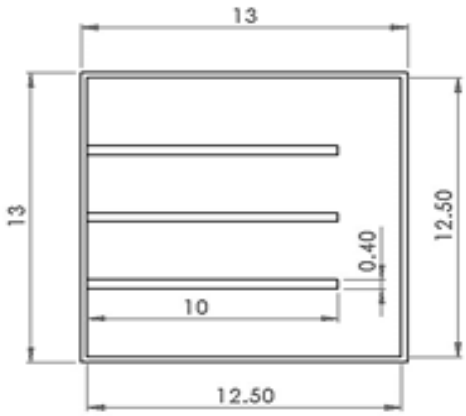

Figure 3: Schematic of Flat Fins-3D.

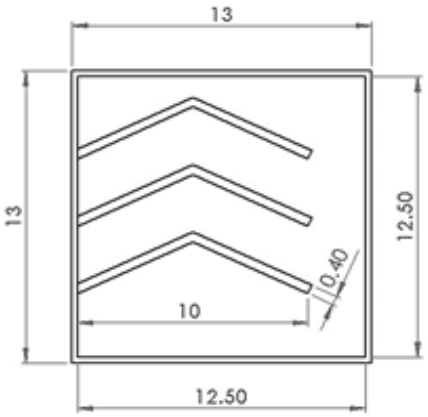

Figure 4: Schematic of Corrugated Fins-3D.

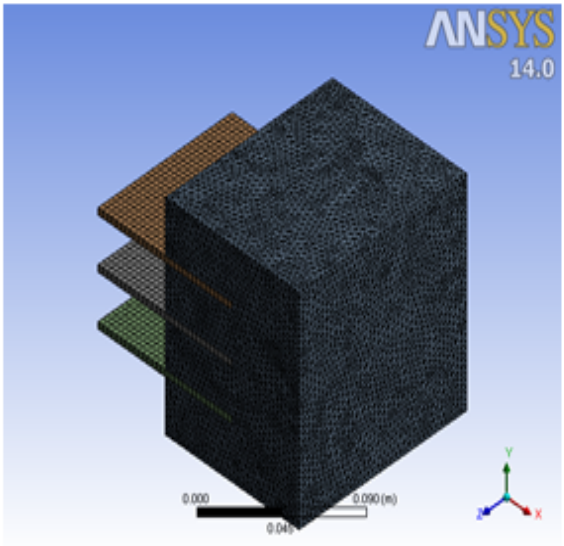

Figure 5: Mesh of Flat Fins.

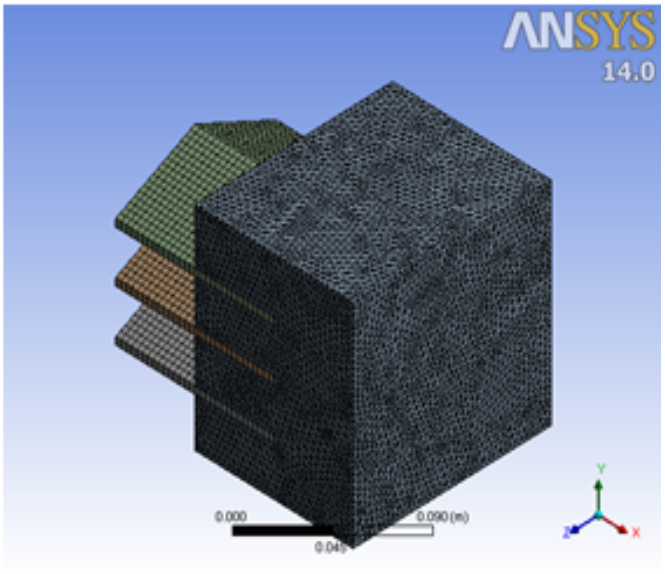

Figure 6: Mesh of Angular Corrugated Fins.

Laminar flow characteristics were setup in Fluent for each analysis conducted. Energy equations were ON to define heat transfer within the models setup. The material selected is Stainless Steel. The source term for heat enable and edit had the value of 1666750 W/m^3 for flat fin and 1540790.4 W/m^3 for triangular fin under zone conditions setup.

2.2 Experimental Setup

The main requirement for the experiment is to maintain a controlled atmosphere. Experimental setup was conducted in an air-conditioned lab. Figure 7 shows the experimental setup used in the current study; the parts of the equipment used are listed below. Figures 8 and 9 illustrate the fabricated flat fins and the corrugated fins respectively.

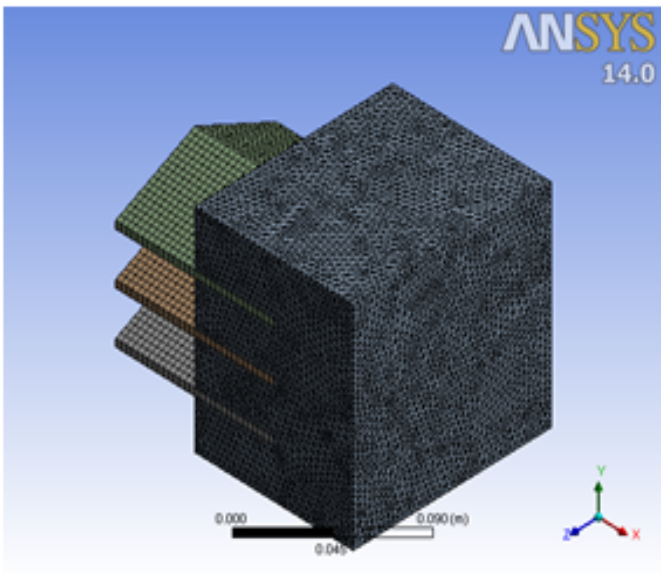

Figure 7: Experimental setup (Heat Convection Trainer-Model: TERA-CT-115.

1. Control Panel.
2. Heater Power Source Control.
3. Heat Power Source Socket.
4. Thermocouple-Air Outlet (2pcs).
5. Ducting-Exhaust Section.
6. Digital Thermometer.
7. Fin Outlet (1pc).
8. Interchangeable Heater Section.
9. Thermocouple-Fin Inlet (1pc).
10. Thermocouple-Air Inlet (2pcs).
11. Ducting-Intake Section.
12. Anemometer.
13. Thermocouple-Room (1pc).
14. Axial Fan.
15. Air Intake Control Valve.

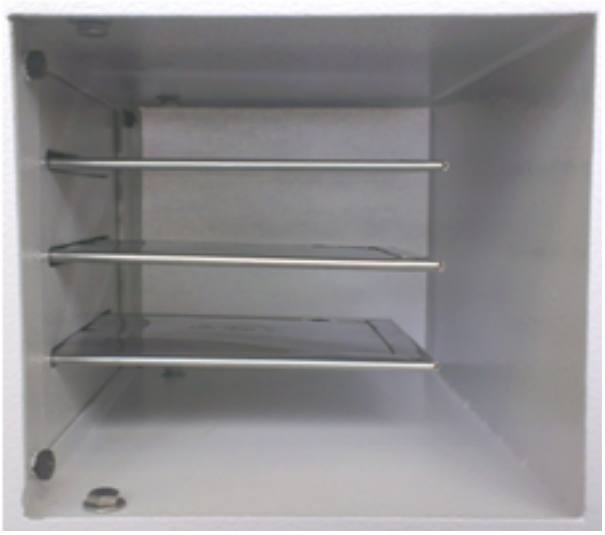

Figure 8: Fabrication Design for Flat Fins.

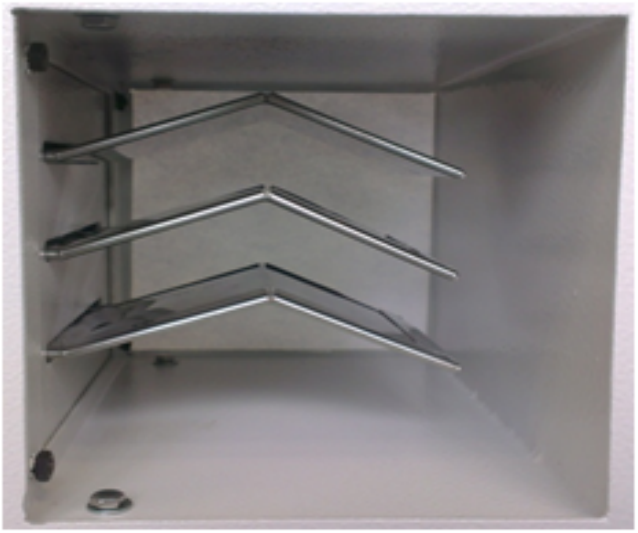

Figure 9: Fabrication Design for Angular Fins under boundary conditions setup.

2.3 Experimental Procedures

Heat transfer experiments were conducted in following sequence:

First the Convection Heat Transfer Rig is connected to a 240 V AC single phase power source at then turn on the main switch from the control panel. Then ducting with heater box is inserted and observe the temperature without any heat generator is obtained. The temperature values are measured by the digital thermometer thermocouple sensors.

Switch on the fan and let the air run in the ducting for 5 minutes until the steady state condition is established and measure the air velocity by the anemometer prop where it is fitted into the ducting. The air velocity can be adjustable by the air inlet control valve.

Switch on the heater using the heater switch in control panel and then increase the heater power to 40% for 5 minutes, up to 60% for 5 minutes; at then increase it further to 90% for 20 minutes. During the given time period, record the first temperature data values for the air inlet and outlet as well as for the fin inlet and outlet temperatures, keep the heater at 90% for 5 minutes more to record the second data reading. Record the temperature values as well as the velocity in the data base sheet. It is not advisable to keep the heater at 100% to avoid any damage to the fins.

When the experiment is completed the heater is switched off first and the apparatus is allowed to cool for 5 or 10 minutes before the fan is switched off. The steps are repeated for several times with other heaters.

3 Results and Disussion

The results obtained from the simulation and experimental work carried out using the parameters defined above are shown below in Figures 10 and 11.

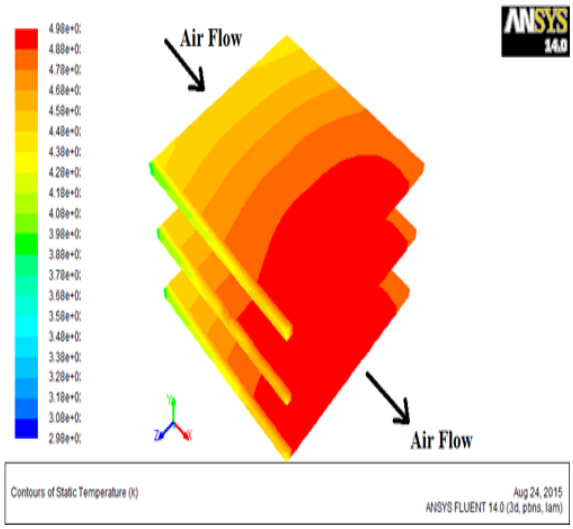

Figure 10: Static Temperature for Flat Fins.

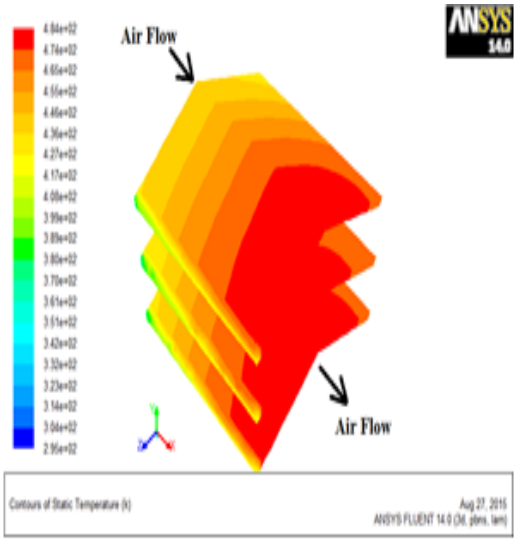

Figure 11: Static Temperature for Angular Corrugated Fins.

Table 1: Temperature comparison results from the simulation.

Design	Minimum Temperature (K)	Maximum Temperature (K)
Flat Fins	298	498
Angular Fins	295	484

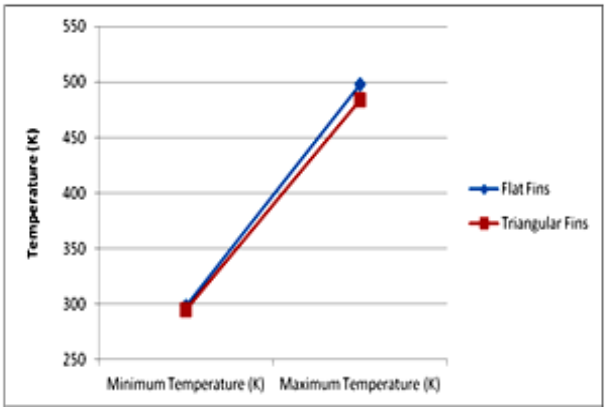

Figure 12: Temperature Comparison Results from the Simulation.

Table 2: Temperature comparison results from experiments.

Type	Minimum Temperature (K)	Maximum Temperature (K)
Flat	300.3	461.1
Angular	300.42	440.0

Based on the results obtained and as shown in figure 12, it has been observed that the angular shape with 484 K temperature is better than the flat shape with 498 K. The maximum temperature difference between both shapes was found to be 2.85%. Thus, it can be concluded that the angular fin with larger surface area has the higher cooling effect than the flat fin at constant velocity and temperature.

3.1 Experimental Results

Results were obtained from the experiments that were conducted several times in order to have stable data. The experimental results shown in Figure 13 illustrate that the maximum temperature for triangular fin was 461 K and for the flat fin was 440 K, with a temperature difference of 4.68%. It was found that the experimental results were similar in pattern with the simulation results as mentioned in table 1. The experimental results are tabulated in Table 2 which shows the temperature behavior for each type of the fins.

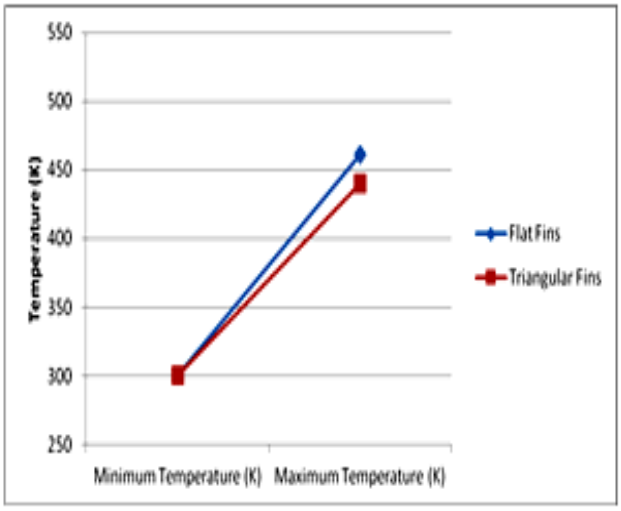

Figure 13: Temperature Comparison Results from Experiments.

3.2 Discussion

Based on the result obtained and as shown in figure 12, it is proven that the best fin shape with higher heat dissipation was achieved under corrugated fin than the flat fin. Therefore, the corrugation profiled fins with increased surface area could obtain the higher heat transfer rate compared to that of a flat fin. As experiments were conducted within the same boundary conditions and specified inlet velocity for various fin shapes, it has been proven that the heat dissipation has direct relation with corrugated fins.

4 Conclusion

In conclusion, CFD simulation and experimental work were carried out for the flat fin and corrugated fin to investigate the heat dissipation capacity. Enhanced heat dissipation was noted under corrugated fins due to increased surface area in comparison with flat fins. The effect of corrugated angular fins has been found to be 4.68% less than the flat fin in the temperature difference. Thus it can be concluded that the corrugated profiled fins

have an improved heat dissipation and would be efficient in heat transfer applications.

References

[1] P. K. Kasana, "Computation of Heat Transfer Augmentation in a plate-fin heat Exchanger using Rectangular/Delta Wing", KURUKSHETRA-136119, India, 2010.

[2] Y. A. Cengel, "Heat and Mass Transfer: (SI Units): A Practical Approach", 3rd edition, 2006.

[3] G. Jogi Nikhil and M. Lawankar Shailendra, "Heat transfer analysis of corrugated plate heat exchanger of different plate geometry: A review", IJETAE, vol. 2, pp. 110-115, 2012.

[4] Tisekar Salman, A. Mukadam Shakeb, Vedapathak Harshad S, Rasal Priyanka K and Khandekar S.B, "Performance analysis of corrugated plate heat exchanger with water as working fluid", IJRET, vol. 5, pp. 56-62, 2016.

[5] Khoshvaght Aliabadi, Khoshvaght and Rahnama, "Thermal hydraulic characteristics of plate fin heat exchangers with corrugated/vortex-generator plate fin (CVGPF)", Applied Thermal Engineering, vol. 98, pp. 690-701, 2016.

[6] Zhao Gang Qi, Jiang Ping Chen and Zhi Jiu Chen, "Parametric study on the performance of a heat exchanger with corrugated louvered fins", Applied Thermal Engineering, Vol. 27, pp. 539-544, 2006.

[7] Kijung Ryu and Kwan Soo Lee, "Generalized heat transfer and fluid flow correlations for corrugated louvered fins", Int. J. of heat and mass transfer, Vol. 83, pp. 604-612, 2015.

[8] Kijung Ryu and Kwan Soo Lee, "Optimal design of a corrugated louvered fin", Applied thermal engineering, vol. 68, pp.76-79, 2014.

[9] Jang Won Seo, Chanyong Cho, Sangrae Lee and Young Don Choi, "Thermal characteristics of a primary surface heat exchanger with corrugated channels", Entropy, vol. 18, pp. 1-16, 2015.

[10] D. Kumbhar, N. K. Sane and C. S. T, "Finite Element Analysis and Experimental Study of Convective Heat Transfer Augmentation from Horizontal Rectangular Fin by Triangular Perforations," in Int. Conference on Advances in Mechanical Engineering, Gujarat, 2009.

Research Paper

Study of Effect of Heat Treatment Processes On Material Properties of Manganese Steels

G. Sandesh Kumar Rai[1], Vishwanatha Nayak[2], Ravindra Mallya[1], J. Rohith Acharya[1], P. Rajesh Rai[3]
[1]Mechanical Engineering Dept., Canara Engineering College, Bantwal, Mangalore-574219
[2]Mangalore Marine College and Technology Kuppepadavu Post, Mangalore, Karnataka 574144
[3]AJ Institute of Engineering and Technology, Bangrakuloor, Kodikal, Mangalore, Karnataka 575013
Email:sandeshkumarrai@gmail.com

Abstract

Heat treatment on manganese steel improves ductility, toughness, hardness and tensile strength and to relieve internal stress developed in the material. The hardness test, impact test, wear test, compression test and microstructure analysis were conducted on heat treated manganese steel, which has extensive uses in all industries including electronic, research and development fields.

The manganese steel properties can be varied with the various heat treatment processes such as annealing, tempering, normalising, hardening and spheroidising. The material is given a micro finish for performing the microstructure analysis. The micro finish of the heat-treated specimen was super-finished in the single disc polishing machine. The polished specimens were etched for finding the exact microstructure. The optical microstructure images were taken at different magnifications and were studied.

The test results show that tempering can be done to increase the toughness, annealing can be done to increase the toughness and ductility, normalising can be done to improve the hardness with some ductility and spheroidising to increase the machinability.

Keywords:-annealing, charpy test, hardening, normalizing, spheroidising and tempering.

1 Introduction

Steel has many practical applications in every aspect of life. The manganese steel is very important material for the industries working on metals including electronics. Manganese is hard and very brittle, difficult to fuse, but easy to oxidize. Manganese steel having manganese content of 1-1.5% makes the steel strong and tough and manganese content from 2-5% makes the steel hard and brittle. When manganese is from 11-14%, steel becomes very hard, tough, and nonmagnetic and possesses considerably high tensile strength. Manganese steel shows high percentage of elongation. It can be forged easily but difficult to be machined. Specific gravity of manganese steel is 7.2, melting point 1343°C. Compositions of manganese steel are: Carbon 1.2-1.6%, Manganese 11-14%, Chromium 1.5-2.5% and Silicon 0.5%.

The manganese content in carbon steels is often increased for the purpose of increasing hardening and improving strength and toughness. Manganese is a silvery-gray metal resembling iron. Manganese is present in all steels as a de-oxidizer. When manganese is absent or very low, the predominant sulphide is iron sulphide (FeS), which forms the eutectic with iron, has affinity to form thin continuous films around the primary crystals during solidification of the steel. A higher content of manganese in the presence of carbon substantially increases the wear resistance.

The process of heat treatment is carried out first by heating the metal and then cooling it in water, air, oil and brine water. The purpose of heat treatment is to soften the metal, to change the grain size, to modify the structure of the material and relieve the stress in the material. The various heat treatment processes are annealing, normalizing, hardening, tempering and spheroidising.

Heat Treatment is the controlled heating and cooling of metals to alter their physical and mechanical properties without changing the product shape.

The most important heat treatments and their purposes are:

a) Normalizing - it will improve strength along with some ductility;

b) Surface hardening - Produces a local wear resistant hard surface by induction, flame, or laser;

c) Hardening and tempering - it will increase hardness and gives improved strength and higher proof stress ratio;

d) Stress relieving - to reduce or relieve Internal stresses remained after casting and a low-temperature heat treatment;

e) Austempering - it will yield to give bainitic structures of high strength along with significant ductility and good wear resistance;

f) Annealing - It will improve ductility and toughness and reduce hardness.

L.A. Dobrzanski et al [1] have investigated high-manganese austenitic steels with Nb and Ti microadditions in variable conditions of hot-working, which showed microstructure evolution in various conditions of plastic deformation. Microstructure of steel was subjected to solution heat treatment at temperature of 900°C and obtained fine-grained microstructure of austenite phase.

In their subsequent work [2] they have determined the force-energetic parameters of hot-working in hot-compression tests carried out in a temperature range

of 850 to 1050°C. They reported that the dynamic recrystallization leads to structure refinement at temperature 850°C.

J. Adamczyk et al [3] have determined the influence of the initial structure and heat treatment conditions on mechanical properties of DP-type steel. They have realized DP-type structure of desirable ferrite and martensite fractions by heat treatment of the low-carbon steel. Mechanical properties were determined by means of tensile test. They have reported that heat treatment conditions can be useful for manufacturing DP-type steel sheets of high strength and ductile properties and a good suitability for metalforming operations.

K.D. Clarke et al [4] have studied the induction hardening heat treatments using dilatometry on 5150 steel with ferrite-pearlite and tempered martensite initial microstructures to assess effects of prior microstructure and heating rate. They opined that transformation temperatures are significantly higher for a ferrite-pearlite initial microstructure than for a tempered martensite prior microstructure. They have found that maximum hardness is independent of starting microstructure, for a given thermal cycle.

L.A. Dobrzanski et al [5] have determined the influence of hot-working conditions on microstructure evolution and phase composition of high-manganese austenitic steels. They found that steels have a fine-grained austenite microstructure with many twins at an annealing temperature of about 1000°C. This microstructure of steel can be useful in determining power-force parameters for hot-rolling of sheets.

2 Experimental

The experimental procedures adopted for this research work can be listed as follows:
Specimen preparation
Heat treatment
Hardness measurement
Impact testing
Wear measurement
Compression strength measurement
Microstructure study

The specimens were prepared from grade 3 manganese steel based on required volume of material. The properties can be varied with the various heat treatment processes such as annealing, tempering, normalising, hardening and spheroidising which were carried out on manganese steel by varying the soaking time of each heat treatment to three different timings i.e., 30,45 and 60 min.

The heat-treated materials were then subjected to different material testing processes like hardness test, compression test, wear test and impact test. Vickers hardness testing machine is used for finding the hardness, pin on disc machine for wear test, Charpy impact testing machine to find the impact strength and universal testing machine (UTM) is used to find the compression strength. The material testing is done for the entire specimens with different heat treatment processes and also for the specimens without heat treatment.

Microstructure analysis and metallography are usually conducted to determine the material's response to thermal heat treatment. The sample to be studied is often wet abrasive sectioned, cleaned and mounted in bakelite or a resin to hold it during grinding and polishing.

Later the material is given a micro finish for performing the micro structure analysis. The surface of the heat treated specimen was super finished in the single disc polishing machine. The polished specimens are etched for finding the exact micro structure. The microstructure was studied at different magnifications.

3 Results and Discussions

3.1 Test results

The hardness test, compression test, wear test and impact test were conducted on these manganese steel test specimens before and after heat treatment processes. The material testing like compression test, impact test, wear test, hardness tests and microstructure analysis were conducted to find the effect of heat treatment process on the specimens. The values were calculated and tabulated in Table 1.

Table 1: Vickers hardness test specification before heat-treatment.

Load (kgf)	30
Diameter (d1) (mm)	0.440
Diameter (d2)(mm)	0.439
Mean diameter (d)(mm)	0.439
Vickers Hardness Number (VHN)	286.42

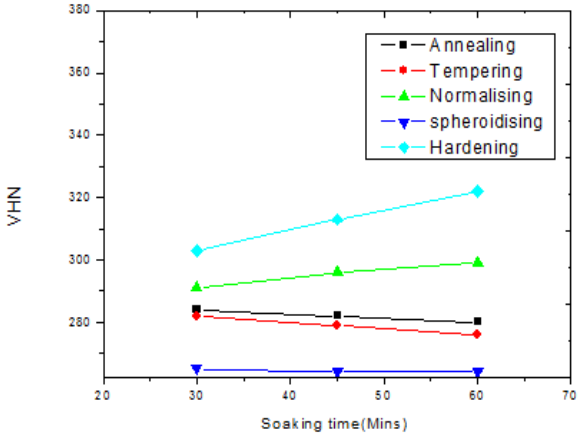

Figure 1: Variation of VHN with soaking time.

Figure 1 shows hardness of specimens under various heat treatment processes. Spherodising process makes the material softer. Hardening process makes the material harder with soaking time and all other processes come in between.

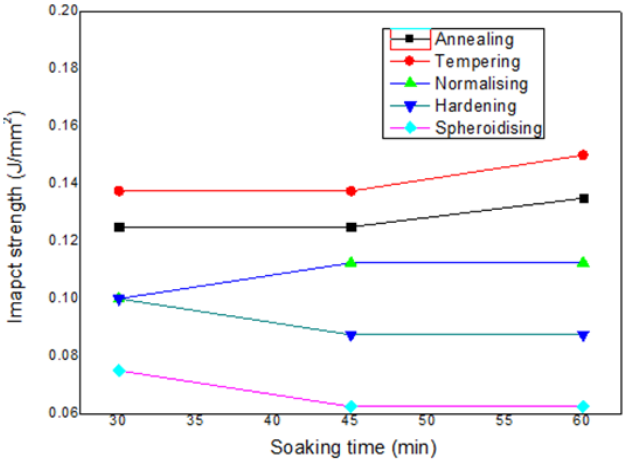

Figure 2: Variation of impact strength with soaking time after heat treatment.

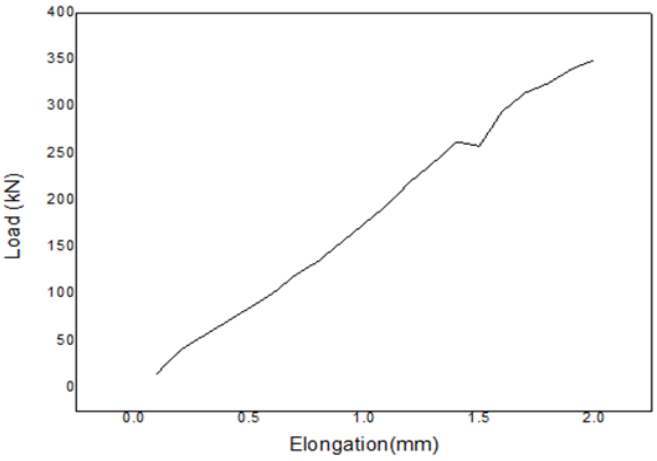

Figure 4: Variation of load with elongation of the specimen without heat treatment under compression test.

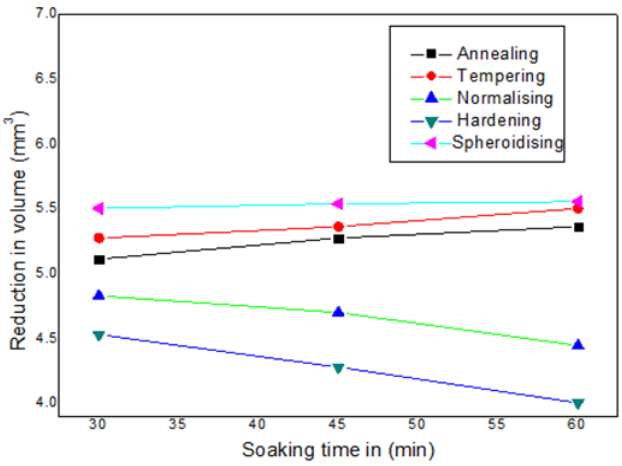

Figure 3: Variation of reduction in volume with soaking time.

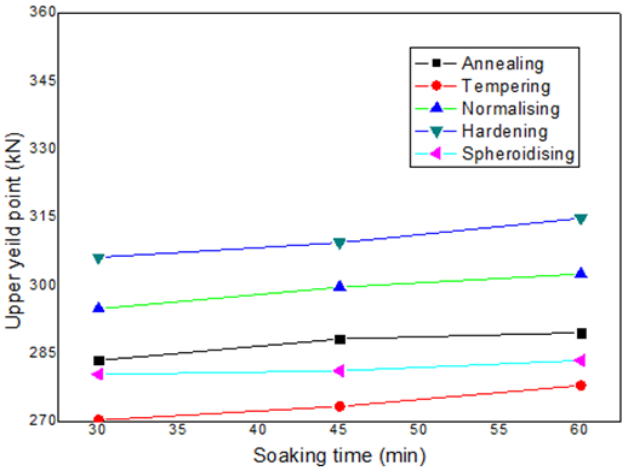

Figure 5: Variation of upper yield point with soaking time after heat treatment.

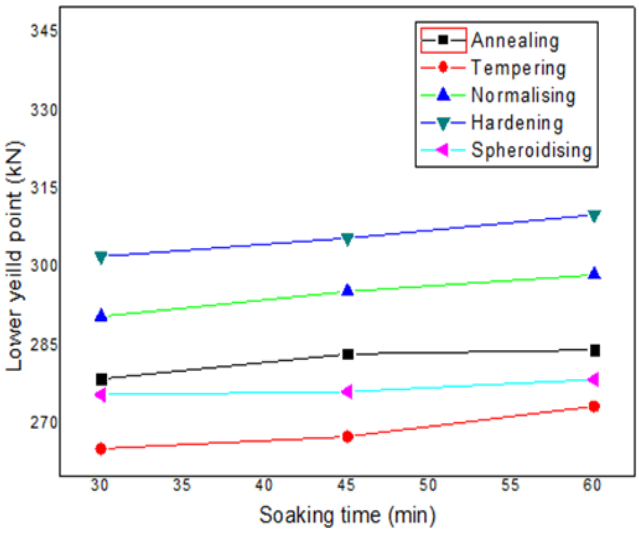

Figure 6: Variation of lower yield point with soaking time after heat treatment.

The Impact strength (J/mm^2) before heat treatment was tested and found to be 0.1 J/mm.^{2} Shown in figure 2 is variation of impact strength with soaking time after heat treatment. From figure 2 it is clear that spherodising process gives low impact strength to the material. The tempering process gives high impact strength to the material and the strength increases with increasing soaking time, all other processes are seen in between.

Figure 3 reveals that spherodising process makes the material softer which results in increase in wear or reduction in volume. Hardening process makes the material harder and decreases the wear of the materials with increasing soaking time. All other processes come in between.

Figure 4 shows the variation of load with elongation of

the specimen without heat-treatment under compression test. It is seen from the figure that upper yield point is 262.24 kN and lower yield point is 257.64 kN. Figure 5 shows the upper yield point in a compression test of specimens under various heat treatment processes. Tempering process decreases the compression strength of the material. Hardening process increases the compression strength of the material with increasing soaking time. Figure 6 shows lower yield point in a compression test of specimens under various heat treatment processes. Tempering process decreases the compression strength of the material. Hardening process increases the compression strength of the material with increasing soaking time. All other process come in between.

3.2 Microstructure Analysis

Figure 7 shows Optical microstructure of manganese steel before and after heat-treatment for 30,45 and 60 min. α-ferrite and pearlite phases, are seen; the pearlite structure is distributed in α-ferrite.

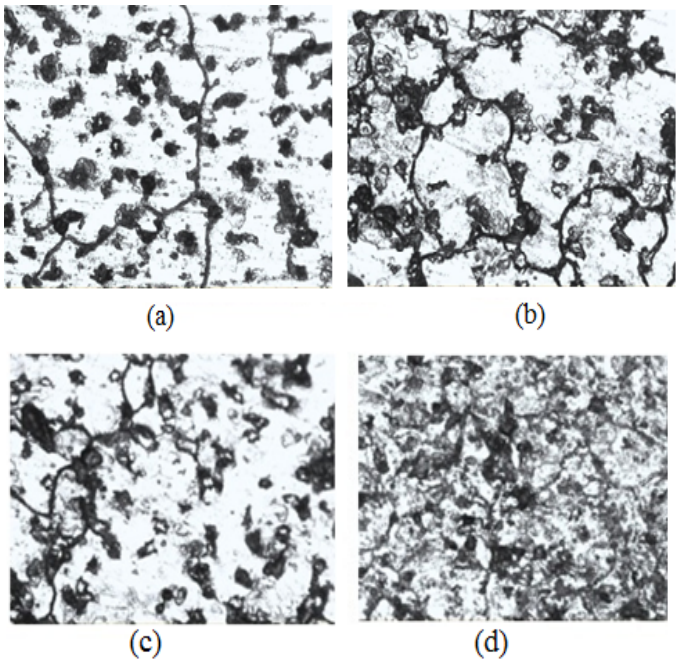

Figure 7: Optical microstructure of manganese steel:
(a) without heat treatment;
(b) after annealing with 30min. soaking time;
(c) after annealing with 45min. soaking time;
(d) after annealing with 60min. soaking time.

In figure 7 (d) the α-ferrite and pearlite phases are evenly distributed and are denser than that for 30 and 45 minutes of soaking. The property of the pearlite phase is to improve the toughness of the steel and reduce the hardness which is seen in microstructure after annealing with 60min. soaking time.

In figure 8 the α-ferrite and pearlite matrix is seen clearly. The property of the pearlite is to improve the toughness and α-ferrite is to improve the mechanical property. Thus, tempering reduces the hardness and improves toughness of the materials which is seen after tempering with 60 minutes of soaking time. The toughness increased when compared with 30 minutes of soaking time.

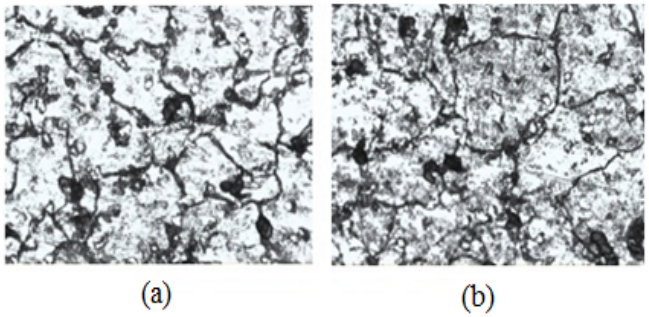

Figure 8: Optical microstructure of manganese steel:
(a)after tempering with 30min. soaking time;
(b)after tempering with 60min. soaking time.

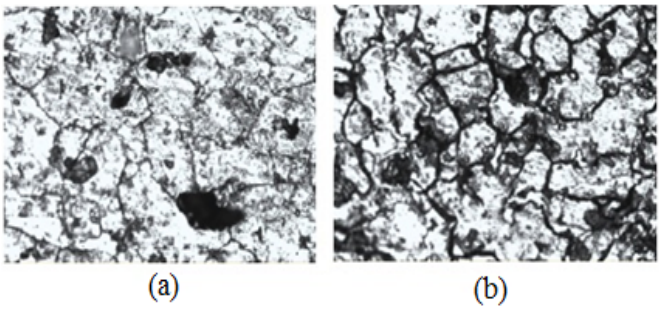

Figure 9: Optical microstructure of manganese steel:
(a) after hardening with 30min. soaking time;
(b) after hardening with 60min. soaking time.

The α-ferrite and pearlite in martensite matrix is seen in figure 9(a). The property of the martensite is to improve the hardness of the material. The hardness of the material is due to the presence of martensite as seen in microstructure after hardening with 30 minutes of soaking time. The Martensite reduces the toughness.

Figure 9(b) shows the presence of α-ferrite and pearlite in martensite matrix. The martensite found in figure 9(a) is denser than the martensite seen in hardening with 60 minutes soaking time. The property of the martensite is to improve the hardness. And it is seen in the figure that soaking increases the hardness of the material and the increase in hardness is due to the presence of martensite phase.

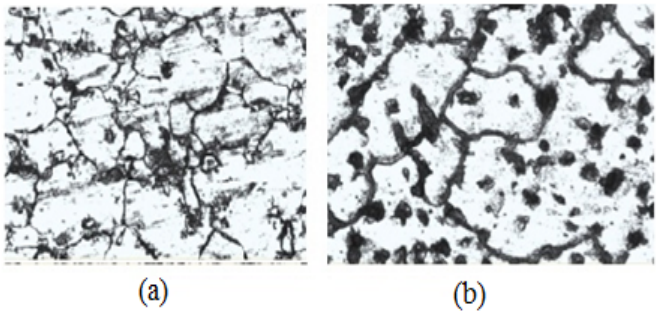

Figure 10: Optical microstructure of manganese steel:
(a) after normalising with 30min. soaking time;
(b) after normalising with 60min. soaking time.

Figure 10 shows the normalising behaviour of manganese steel. The distributed pearlite with martensite matrix is seen in figure. The property of martensite is to improve the hardness and the pearlite to improve the toughness. It is seen in the result that normalising increases the hardness, wear resistance and toughness of the manganese steels with the increase of soaking time.

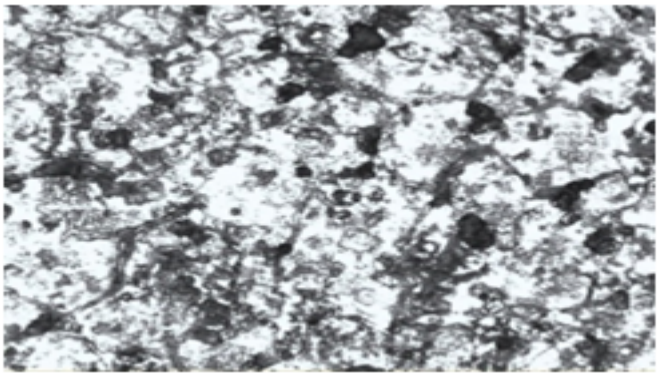

Figure 11: Optical microstructure of manganese steel after spheroidising for 60 min.

Figure 11 shows the optical microstructure after spheroidising where pearlite or graphite granules in α-ferrite are seen. The properties of granules are to reduce the hardness of the material. So, it is seen from the result that spheroidising reduces hardness, which can be used to improve the machinability of the manganese steel.

4 Conclusion

From various results obtained during this work it can be concluded that heat treatment mainly improves the hardness of the manganese steel; it is found from the observations that the hardness increases as the soaking time increases. Similarly, the hardening increases wear strength, impact strength and also yield strength of the manganese steel with increasing soaking time. Hence, hardening can be used to improve the mechanical properties of manganese steel.

The tempering heat treatment process is used for increasing the strength, with significant ductility and good wear resistance. From the result obtained after tempering it is found that hardness, wear strength, impact strength and yield strength of the manganese steel also increase with increase in soaking time. But the change in the mechanical properties after tempering is comparatively lower when compared with the hardening heat treatment.

The normalising heat treatment is carried out mainly to improve strength with some ductility. From the results obtained after normalising it is found that hardness, wear strength, impact strength and yield strength of manganese steel also increases with increase in soaking time. But the increase in these mechanical properties is comparatively lower when compared with hardening and tempering heat treatment processes.

The annealing heat treatment process is carried out to reduce hardness and to improve machinability such as to facilitate cold working. From the results obtained after annealing it is found that hardness, wear strength and impact strength of manganese steel decreases with increase in soaking time. But the yield strength increases with increase in soaking time. The Spheroidising heat treatment process is also carried out to improve machinability. From the results obtained after annealing it is found that hardness, wear strength and impact strength of manganese steel decreases with increase in soaking time. But the yield strength increases with increase in soaking time. Hence, to improve machinability, the spheroidising heat treatment should be carried out on manganese steel.

References

[1] L. A. Dobrzanski, A. Grajcar and W. Borek, "Influence of hot-working conditions on a structure of high-manganese austenitic steels", J. Achievements in Materials and Manufacturing Engineering, vol. 29, pp. 139-142, 2008.

[2] L. A. Dobrzanski, A. Grajcar and W. Borek, "Hot-working behaviour of high-manganese austenitic steels", J. Achievements in Materials and Manufacturing Engineering, vol. 31, pp. 7-14, 2008.

[3] J. Adamczyk and A. Grajcar, "Effect of heat treatment conditions on the structure and mechanical properties of DP-type steel", J. Achievements in Materials and Manufacturing Engineering, vol. 17, pp. 305-308, 2006.

[4] K. D. Clarke, C. J. Van Tyne, C. J. Vigil and R. E. Hackenberg "Induction hardening 5150 steel: effects of initial microstructure and heating rate", J. Materials Engineering and Performance, vol. 20, pp. 161-168, 2011.

[5] L. A. Dobrzanski, A. Grajcar and W. Borek, "Microstructure evolution and phase composition of high-manganese austenitic steels", J. Achievements in Materials and Manufacturing Engineering, vol. 31, pp. 218-225, 2008.

Scientific Article

Search for the value of π – A brief history

A. Jayarama[1] and Richard Pinto[2*]
[1]Physics Dept., Sahyadri College of Engineering & Management, Adyar, Mangalore-575007
[2]E & C Dept., Sahyadri College of Engineering & Management, Adyar, Mangalore-575007
*Email:director.cent@sahyadri.edu.in

The calculation of the ratio between perimeter of a circle and its diameter, which is known by the Greek letter π, has been one of the most enduring challenges in mathematics.

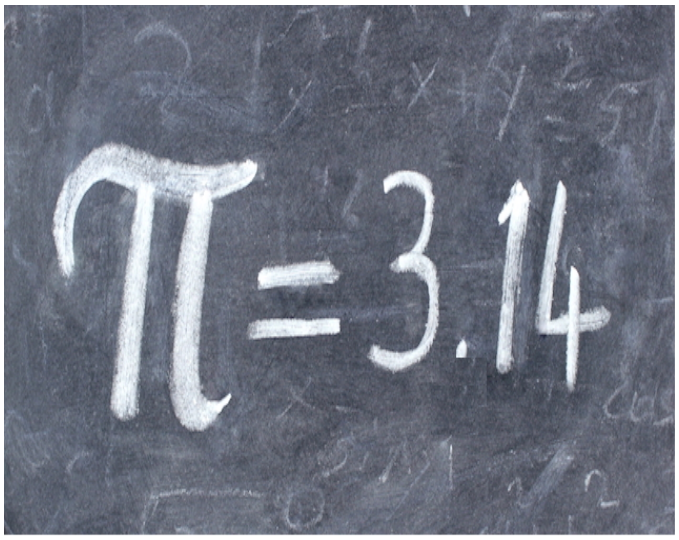

From ancient Babylonia, Egypt, China, India, Middle Ages in Europe and to the present day supercomputers, mathematicians have been trying to calculate the value of π which has evoked much mystery, romanticism and interest. Although we may never know the origin of π, the people who initiated the hunt for the value of π were the Babylonians and Egyptians, who measured experimentally the ratio of the perimeter and diameter of a circle with a string nearly 4000 years ago. Antiphon and Bryson, in ancient Greece, took up the problem with an innovative idea of fitting a polygon inside a circle, calculating its area, and doubling the sides repeatedly. However, their work resulted in finding the areas of many tiny triangles, which was not only complicated but also resulted in few digits [1]. The first Greek whose work initiated a major impact in the calculation of π was Archimedes of Syracuse. Unlike Antiphon and Bryson, Archimedes took up the challenge by focusing on the perimeter of polygons as opposed to their areas and approximated the circumference of the circle instead of its area. He inscribed a hexagon in a circle and doubled its sides four times to finish with a 96-sided polygon; after numerous calculations he ended with a result:
$3\ 10/71 < \pi < 3\ 1/7$ which has lower and upper bounds for the value of π [2]. While the earliest value of π considered in China was 3, Liu Hui independently calculated, in 263 AD, the perimeters of regular inscribed polygons with upto 192 sides, and derived the value $= 3.14159$, which is accurate to the first five digits; this is similar to the method used by Bryson and Antiphon hundreds of years earlier in Greece. Subsequently, Tsu Chung-chih and his son Tsu Keng-chih, at the end of the 5^{th} century calculated the value of π by using inscribed polygons with 24,576 sides and came up with upper and lower bounds as $3.1415926 < \pi < 3.1415927$! [1] Later, Aryabhata from India gave the 'precise' value $62{,}832/20{,}000 = 3.1416$ [3]. Soon after, Brahmagupta, another Indian mathematician, used a novel approach by calculating the perimeters of polygons inscribed in a circle and postulated that the value of π would approach the square root of 10 [=3.162...]. In Europe in 1593, Adrianus Romanus used an inscribed polygon with 230 sides to calculate value of π upto 17 digits. Later, Ludolph Van Ceule from Germany used the Archimedes's method of polygons with over 500 million sides and came up with 20 digits; moving on, in 1610, he calculated value of π accurate to 35 digits. His accomplishments, realized without the use of a modern computer, were considered so important that the digits were engraved on his tombstone in St. Peter's Churchyard in Leyden [4].

In twentieth century, D. F. Ferguson discovered an earlier error (1873) in William Shanks calculation of value of π from the 528^{th} digit onward. In 1947, he presented the results of his calculations with 808 digits of π [5]. Later, Levi Smith and John Wrench achieved the 1000-digit-mark [5]. A new breakthrough which emerged in 1949 is with the invention of ENIAC (Electronic Numerical Integrator and Computer); using punch cards and ENIAC, a group of mathematicians calculated 2037 digits in just seventy hours [3]. The advent of the electronic computer in the 1970s resulted in a race to find the accurate value of π [1]. A breakthrough occurred in 1976 when Eugene Salamin found an algorithm which doubles the number of precise digits with each iteration; this is an improvement over the previous formulae which only added a few digits per calculation [1]. Over the next twenty years many researchers worked together and led the way throughout the 1980s, until in August 1989 David and Gregory Chudnovsky broke the one-billion-digit-barrier. Kanada and Takahashi in 1997, calculated 51.5 billion digits in just over 29 hours, which means an average rate of about 500,000 digits per second!. This was further improved by them in 1999 to 68,719,470,000 digits. [1]. The question is whether calculation of π to the n^{th} digit (where n > one billion) is really necessary?? Just 39 decimal places would be sufficient to calculate the perimeter of a circle surrounding the known universe with a precision of the radius of a hydrogen atom!! At the present time, it appears that the only tangible application

of all those digits is to find the bugs in computer chips and computers. Further, mathematicians are also looking for the occurrence of some rules that will distinguish the digits of π from other numbers. But, Chudnovskys have also opined that no other calculated number comes close to a random sequence of digits other than that of magical number π.

References

[1] David Blatner, "The Joy of Pi", Walker Publishing Co., Inc., New York, 1997.

[2] https://www.math.rutgers.edu/ cherlin/History/Papers 2000/wilson.html.

[3] Petr. Beckman, "The History of Pi", The Golem Press. Boulder, Colorado, 1971.

[4] Florian Cajori, "A History of Mathematics", MacMillan and Co., London, 1926.

[5] Lennart Berggren, Jonathan Borwein and Peter Borwein, "Pi: A Source Book", Springer-Verlag. New York, 1997.

Sahyadri International Journal of Research

Guidelines for Submission

- Authors are requested to provide full details for correspondence: postal address, phone numbers and email address. (The email address of corresponding authors will be published along with the article).
- Authors are requested to prepare their soft copy version in text formats and not in PDF version.
- Authors are requested to follow the manuscript template while preparing the manuscript.

SIJR is devoted to the publication of original research work. The journal also accepts review papers and scientific articles. SIJR welcomes the submission of manuscripts that meet the journal standard which includes novelty, significance and excellence. Every volume of the journal will have two issue in a year. All articles published in the SIJR are peer-reviewed.

Contact for any query or Information on
SAHYADRI International Journal of Research
Dr. Richard Pinto - Editor-in-Chief
or
Dr. Jayarama A - Editor
Email: editor@sijr.in
Web: www.sijr.in

Publisher
Manjunath Bhandary - President
Bhandary Foundation, Sahyadri Campus, Adyar, Mangaluru - 575 007

Printers
Prakash Offset Printers, 164, Industrial Area, Baikampady, Mangaluru - 575 011

Sahyadri campus - The sprawling campus just off the Mangalore-Bangalore National Highway 48 is situated on the banks of the river Nethravathi. Surrounded with natures pristine beauty and an excellent infrastructure coupled with dedicated and experienced faculty has made the Campus a much sought-after abode of learning.

Empowering young minds

SAHYADRI

COLLEGE OF ENGINEERING & MANAGEMENT

(Affiliated to VTU, Belagavi and Approved by AICTE, New Delhi)

Sahyadri Campus, Adyar, Mangaluru - 575 007

+ 91-824-2277222 | + 91 96119 45201 | editor@sijr.in | www.sijr.in | www.sahyadri.edu.in